Chemical Engineering Journal 397 (2020) 125416

Contents lists available at ScienceDirect

Chemical Engineering Journal

journal homepage: www.elsevier.com/locate/cej

Surface coordination of black phosphorene for excellent stability, flame retardancy and thermal conductivity in epoxy resin

Zhencai Qu[a,b], Kun Wu[a,*], Weihua Meng[c], Bingfei Nan[a,b], Zhuorong Hu[a,b], Chang-an Xu[a,b], Zhiyou Tan[a,b], Qian Zhang[a,b], Huifa Meng[a,b], Jun Shi[a]

[a] Guangzhou Institute of Chemistry, Chinese Academy of Sciences, Guangzhou 510650, PR China
[b] University of Chinese Academy of Sciences, Beijing 10049, PR China
[c] College of Chemistry and Environmental Science, Hebei University, Baoding 071002, PR China

HIGHLIGHTS

- Black phosphorene was successfully coordinated by a ruthenium sulfonate ligand.
- Excellent stability in environment was obtained.
- Dramatically improved flame-retardant efficiency was achieved.
- Significantly enhanced thermal conductivity with small amount.

ARTICLE INFO

Keywords:
Black phosphorene
Ruthenium
Surface coordination
Flame-retardancy
Thermal conduction

ABSTRACT

Black phosphorus (BP) are shining for its promising properties. Due to the instability and agglomeration problem, the surface coordination strategy is a key point in practical applications. Herein, a ruthenium sulfonate ligand is synthesized to coordinate black phosphorus (BP) nanosheets. By virtue of Ru-P coordination, the lone pair electrons in BP are occupied, thus the RuL_3@BP displays excellent stability in environment and different solvents. Subsequently, the resulting RuL_3@BP is added into epoxy resin (EP) to fabricate EP nanocomposites. RuL_3@BP can effectively enhance the dispersibility of BP in EP due to the surface coordination. When the RuL_3@BP is added into epoxy in an amount of 3 wt%, the char yield is distinctly improved by 96.83%, which is ascribed to the cooperative catalytic charring effect between BP and RuL_3. EP/RuL_3@BP nanocomposites can easily pass the UL-94 V-0 rating, and its limiting oxygen index (LOI) value rises by 26.72%. The peak of heat release rate (PHRR) is decreased by 62.21% and the total heat release (THR) reduces by 35.22%, which is assigned to the restriction of heat transfer and inhibition of flammable gas by the dense char residues. The smoke production and diffusion of thermal pyrolysis gases are dramatically suppressed in the combustion. Meanwhile, owing to strong interfacial interactions between RuL_3@BP and EP, EP nanocomposites filled with 3 wt% RuL_3@BP exhibit a high thermal conductivity of 0.376 W m^{-1} K^{-1}, which is enhanced by 52.23% and 65.64% compared with that of EP/BP composite (0.247 W m^{-1} K^{-1}) and pure EP (0.227 W m^{-1} K^{-1}), respectively. This surface coordination strategy provides a novel approach for fabricating advanced-performance nanocomposites.

1. Introduction

Black phosphorus (BP), a new candidate of two-dimensional (2D) nanomaterials, has attracted increasing attention in recent years because of its inherent layered structure, distinctive properties and potential applications [1,2]. Due to its weak van der Waals force, BP crystals can be easily stripped into mono- or few-layer BP sheets which are known as “phosphorene” [3]. Similar to other 2D material from their 3D parents, mono- to few-layer BP is principally fabricated by a top-down strategy through the ways of exfoliation, such as microcleavage method [4], ball milling [5,6], electrochemical exfoliation [7], liquid exfoliation with sonication in different solvents [8]. The microcleavage fabrication is the first approach to obtain monolayer phosphorene, but the production is limited, and it is only suitable for fundamental studies [3,9]. By virtue of ball milling method, the mono- and few-layer of BP can be prepared with a low purity and weak

* Corresponding author.
E-mail address: wukun@gic.ac.cn (K. Wu).

https://doi.org/10.1016/j.cej.2020.125416
Received 4 March 2020; Received in revised form 27 April 2020; Accepted 7 May 2020
Available online 11 May 2020
1385-8947/

crystallinity [10]. Electrochemical methods can produce phosphorene faster, but the layer numbers of phosphorene are too thick, which is unfavorable for subsequent applications. Compared with the method described above, liquid phase exfoliation owns the merits of easy operation, low structure damage, high yield and fine performance, and has already become an optimum method for the fabrication of phosphorene. For instance, N-methyl-2-pyrrolidone (NMP) [8], dimethyl sulfoxide (DMSO) [11], N-cyclohexyl-2-pyrrolidone [12] and isopropanol (IPA) [13] are the frequently-used solvent medium to exfoliate the singe- or few-layer of BP. The size and crystallinity of BP can be supervised by the time and power of sonication. Phosphorene is better than conventional 2D nanomaterials such as graphene [14], silicene [15], MoS_2 [16] and silicon carbide [17], as it can offer thickness-tunable bandgap (0.3–2 eV) [18], high charge carrier mobility (up to 1000 $cm^2\ V^{-1}\ s^{-1}$), controllable on/off ratio (10^2-10^5) and broad ultraviolet absorption range [5]. These remarkable properties make BP a shining star which is extensively used in optoelectronic devices, supercapacitors, photocatalysts, hydrogenation, thermoelectric conversion and biomedical fields [19]. Furthermore, the mono- or few-layer BP possesses the characteristic size effects, admirable mechanical properties and high thermodynamic stability, which is expected to become a novel nano-filler to fabricate the advanced-performance polymer composites [20].

In spite of these intriguing performances, an essential obstacle restricting the application of BP is ascribed to the instability of air and water. Many studies have confirmed that BP is highly inclined to oxidation under ambient conditions, resulting in a serious destruction of chemical and physical structure [21]. Long-term exposure of phosphorene to oxygen and water will lead to a complete degradation which severely hinders the application of BP. Therefore, anti-oxidation and stability are very important in the preparation and application of BP. Numerous researchers have focused on improving the air and water stability of phosphorene and have achieved some progress. Wood [22] used aluminum oxide (AlO_x) to cover the surface of black phosphorus by atomic deposition and found that the surface morphology of black phosphorus covered with AlO_x was not changed significantly after 7 days under ambient conditions, its transistor had little changes in conductivity. Kim [23] first coated a 25 nm Al_2O_3 on the surface of black phosphorus, followed by a highly hydrophobic film to form a double-layered protective layer, which made the electrical properties of its device stable more than three months. Lee [24] added $Ti(OC_4H_9)_4$ to a black phosphorus aqueous solution to prepare a TiO_2-modified black phosphorus composite and found that the BP@TiO_2 composite exhibited good stability in photocatalysis. Hu [25] reported a simple way to covalently decorate BP by AIBN and verified that the modification by covalent bond was a useful strategy to protect the stability of BP. Gonzalo Abelln [26] put black phosphorus crystals into a solution of 7,7,8,8-tetracyano-p-dioxane (TCNQ) in tetrahydrofuran to strip for 3 days to prepare non-covalently modified black phosphorus nanosheets, which could greatly improve the stability of phosphorene. Zhao [27] designed a TiL_4 to study the modification of phosphorene by coordination bonds. By means of the empty orbital of titanium atoms, the titanium ligand could occupy the lone-pair electron of black phosphorus, and the TiL_4@BP could be stable in a humid environment for several days. However, although these researches have made some progress to improve the stability of BP, there still exists some fundamental defects such as complex procedures, high cost and the damage of modification on the properties of BP. Therefore, the modification of phosphorene must consider the impact on its properties.

Owing to the advantages of low cost, light weight, good insulation, strong corrosion resistance, stable chemical properties, and easy processing, polymer materials are now widely applied in petrochemical, aerospace, optoelectronic communications, military industry and other fields. However, high flammability has become a crucial obstacle to hinder its practical application, especially in the field of electronic appliances. Referring to previous literatures, many inorganic nanomaterials were employed to improve the flame retardancy of polymer materials, including carbon nanotubes [28], layered hydroxides [29], phosphorus flame retardant [30], montmorillonite [31] and amine compounds [32]. Compared with these nanomaterials, black phosphorene is completely constituted of P elements which is considered as the most important flame retardant element with high efficiency. In addition, as the most thermally stable allotrope of phosphorus, BP has a larger specific surface area, higher thermal stability and puckered structures than red phosphorus and other phosphorus-containing compounds, these unique properties allow BP to obtain flame retardant effects that other flame retardants cannot achieve. Ren [33] incorporated 0.2 wt% of BP into WPU polymers to synthesize a flame-retardant nanocomposites, and found a 2.6% increase in the limiting oxygen index (LOI) and a 10.3% decrease on the peak heat release rate (PHRR). However, poor compatibility between BP and resins seriously restricted the further improvement of flame-retardant performance. Ren [34] developed a novel route to prepare a flame retardant resins using the black phosphorene/graphene (BP/G) as the fillers, when the total addition of BP/G was 3.55 wt%, for the BP/G/WPU composites, the peak release rate (PHRR) decreased by 48.8% and the total heat release (THR) decreased by 38.63%. Nevertheless, this method required the addition of a surfactant and a pretreatment process, which complicated the preparation process. Qiu [35] reported that polyphosphazene (PZN) modified BP flame retardant was prepared by one-step method using hexachlorocyclotriphosphazene and 4,4′-diaminodiphenylmethane as raw materials. The results found that the modification of PZN could significantly improve the stability and flame retardancy of BP. However, the monomer of HCCP contained six chlorine atoms, which would generate poisonous gases in the combustion and caused harm to the environment.

Ruthenium, has an atomic number of 44, is a unique platinum group metal element with very stable physical and chemical properties, and has been used as a catalyst for hydrogenation, isomerization and oxidation reactions. There are empty orbits in the ruthenium atom, which can form complexes with electron donors. Various types of ruthenium complexes have been widely used in the biomedicine and chemical industries. However, to the best of our knowledge, no reports have been found about coordinated phosphorene with ruthenium. Thus, we firstly prepare a ruthenium sulfonate ligand (defined as RuL_3, L representing the sulfonic acid functional group) as shown in Fig. 1(a), then the few layer BP nanosheets is exfoliated from BP crystals and the RuL_3 is employed to coordinate phosphorene to form RuL_3@BP. Finally, the RuL_3@BP is incorporated into epoxy resin to fabricate EP/RuL_3@BP composites (Fig. 1(b)). The stability of RuL_3@BP in humid conditions and the mechanical performance, flame-retardant properties and thermal conductivity of EP/RuL_3@BP nanocomposites are studied by a series of characterization. This work expects to offer a new strategy to functionalize BP and achieve excellent stability, superior flame-retardant efficiency and high thermal conductivity. Such coordinated strategy is in favor of the application of BP and initiate a novel field for the manufacture of advanced-performance nanocomposites.

2. Experimental

2.1. Materials

BP crystal (99.998%) was provided by Kunming Black Phosphorus Technology (China) and stored in an inert atmosphere. Ruthenium acetate (Ru 40–45%) was obtained from Shanghai Macklin Biochemical Co., Ltd. p-toluenesulfonic acid (AR) was purchased from Guangzhou Guanghua Sci-Tec Co., Ltd. DMF (AR), isopropanol (AR), and EtOH (AR) were purchased from Guangzhou Chemical Reagent Co., Ltd. 4,4-Diaminodiphenylmethane (DDM) was supplied by Aladdin Industrial Corporation (China). EP (DGEBA, E-51) was obtained from Nantong Xingchen Synthetic Materials Co., Ltd. (China).

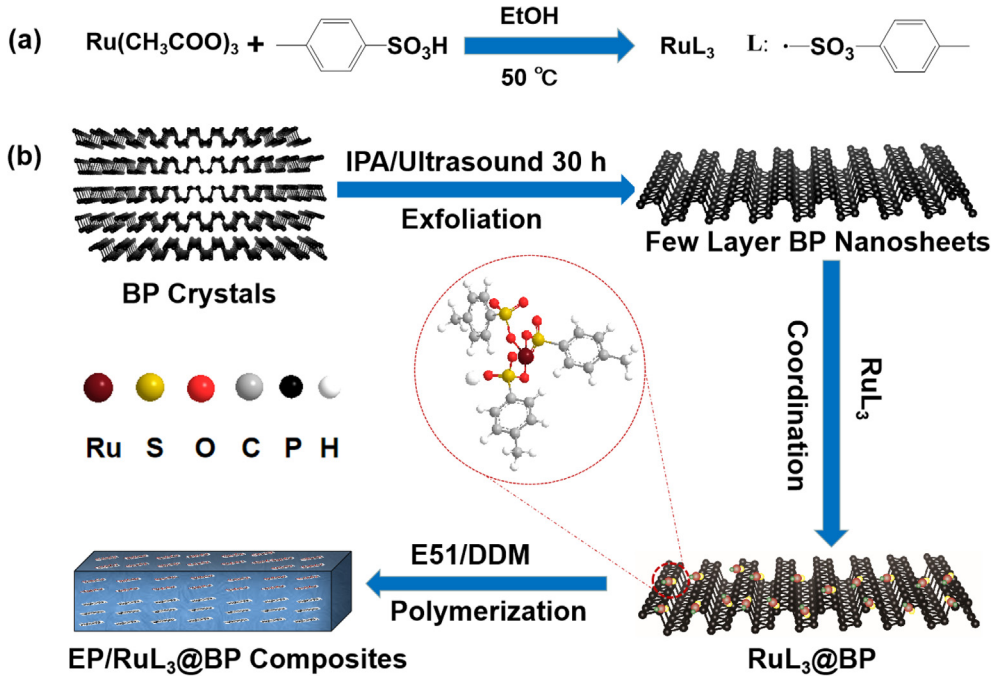

Fig. 1. Preparation of RuL_3 and EP/RuL_3@BP composites: a) synthesis and structural formula of RuL_3; b) fabrication process of RuL_3@BP nano-filler and EP/RuL_3@BP composites.

2.2. Synthesis and preparation

2.2.1. Synthesis of RuL_3

The molar ratios of ruthenium acetate to p-toluenesulfonic acid was 1/3. Firstly, ruthenium acetate was dispersed in EtOH with the assistance of ultrasound (325 W, 15 min) at room temperature. Secondly, p-toluenesulfonic acid was dissolved in EtOH and dropwise added into ruthenium acetate solution. The resultant solution was stirred for 3 h at 300 rpm with the temperature of 50 °C, afterwards, a rotary evaporator was employed to remove the solvent, the products were defined as RuL_3.

2.2.2. Preparation of BP

The BP nanosheets were exfoliated by a liquid phase exfoliation technology. BP crystal (250 mg) was first added into 500 mL of isopropanol (IPA) and sonicated with an ultrasonic cell pulverizer (650 W) for 3 h. The ultrasonic frequency was 20 kHz and the supersonic probe worked for 4 s with a gap time of 6 s. The suspension was then sonicated by an ice bath (325 W) continuously for 30 h. Secondly, the BP dispersion was centrifuged at 2500 rpm for 30 min to get rid of the unexfoliated BP with large sizes. Afterwards, the resulting solutions were centrifuged at 12000 rpm for 30 min, the obtained sediment was dried under vacuum and preserved in an inert atmosphere, which was defined as black phosphorene (BP).

2.2.3. Surface coordination of BP

BP nanosheets (100 mg) were dispersed in IPA (200 mL) with assistance of sonication for 30 min, and then RuL_3 (0.75 g) was added into the BP solution. The mixture was stirred at room temperature for 24 h in darkness under nitrogen atmosphere. Finally, the solvent of the mixture was removed by rotary evaporation, the resultant residue was rinsed with ethanol and dried in a vacuum drying oven at 60 °C. The obtained product was named RuL_3@BP.

2.2.4. Preparation of EP/RuL_3@BP nanocomposites

Fabrication procedure of EP nanocomposites with the incorporation of 1.0 wt% RuL_3@BP as follows: 0.5 g of RuL_3@BP and 9.9 g of DDM were mixed in 30 mL of acetone with the assistance of ultrasound. Then the mixed solutions were dispersed with mechanical stirring for 15 min, afterwards, 39.6 g of epoxy resin (E51) was added into the whole system by mechanical agitation for 30 min. Whereafter, the compound system was put in a vacuum drying oven to remove the solvent at 50 °C for 1.5 h. Finally, the resin composites were cured in a pre-made mold under the process of 100 °C/2h, 150 °C/2h, respectively. When the resultant nanocomposites were cooled to the normal temperature, it was named EP/RuL_3@BP 1.0. Similar procedures were also suitable for pure EP, EP/BP (3.0 wt%) and the content (2.0 wt% and 3.0 wt%) of RuL_3@BP.

2.3. Characterization

Transmission electron microscopy (TEM, Japan, JEM-1230) was used to study the morphology and thickness of BP and RuL_3@BP. Scanning electron microscopy (SEM, JSM 6700, JEOL) was conducted to observe the fracture surface of BP and the char residues of EP/RuL_3@BP nanocomposites. The energy dispersive spectrometer (EDS, JES-FA300, JEOL) was employed to characterize the elements' content and distribution. Atomic force microscopy (AFM) was employed to characterize the layers of BP by a Dimension Icon. Fourier transform infrared spectra (FTIR) was carried out using a TENSOR 27 spectrometer (Bruker) to reflect functional group of RuL_3. The prepared samples were mixed with KBr pellets before characterization. X-ray diffraction (XRD, Bruker D8) were collected with Cu Ka radiation (λ = 0.154 nm), at a scanning rate of 10° min^{-1}. Raman spectra (Raman) was conducted through a Laser micro Raman spectrometer with an argon laser of 530 nm to study the structure of RuL_3@BP and the char residues of EP composites. Thermogravimetric analysis (TGA) was employed with thermo-analyzer instruments (NETZSCH TG 209 F3) in nitrogen atmosphere, with a consecutive heating rate of 10 °C min^{-1} from 30 °C to 800 °C. X-Ray photoelectron spectroscopy (XPS) was employed on a Thermo Fisher Scientific K-Alpha electron spectrometer to observe the element composition with an Al Kα radiation at 1486.8 eV. Optical microscope was employed to observe the dispersity of BP and RuL_3@BP in EP resin, the samples was prepared by rapid slice. Differential scanning calorimetry (DSC, Q200 V24.10 Build 122) was used to test the exothermic peak with a heating rate of 5 °C min^{-1} under the

protection of nitrogen. The tensile stress of composites was measured by an intelligent tensile machine at room temperature with a stretching speed of 2 mm min^{-1}. The thermal images of EP nanocomposites were employed on infrared thermal imager (FLIR ONE PRO) to record the temperature change during heating and cooling process by a LED light strip (24 W). All the samples were cut into a square piece with a size of 10 × 10 × 1 mm for measuring the thermal conductivity. Then, the thermal diffusivity was tested by using an LFA 467 instrument (NETZSCH, Germany). According to the laser flash method, all the samples were measured at 25 °C. In the end, the thermal conductivity was calculated as the following equation: $\lambda = Cp\ \rho\ \alpha$. Where the specific heat capacity (Cp) was conducted by DSC with the sapphire method. ρ was the density and could be calculated through the mass and volume of samples. The thermal diffusion coefficient (α) was carried out by an LFA laser flash apparatus. The method was consistent with the international standard method (ASTM E-1461–13). The combustion performance was measured by a microscale combustion calorimeter (MCC) with a mold of GOVMARK MCC-2. Approximately 3–5 mg of samples were heated under an inert gas atmosphere with a heating rate of 1 °C s^{-1}. Two gases (Nitrogen of 80 mL min^{-1}; Oxygen of 20 mL min^{-1}) were mixed to form the carrier gases and burned at 900 °C. The limiting oxygen index (LOI) and the vertical burning (UL-94) were tested by an oxygen index tester and a vertical burning tester. ^{1}H NMR and ^{13}C NMR were performed by a Bruker instrument (DRX-400, CH_3OH as solution). A UV 2550 spectrometer (Shimadzu) was conducted to detect the dispersion stability of BP and RuL_3@BP in different solvents from 200 nm to 600 nm. Thermogravimetric analysis/infrared spectra (TG-IR) was carried out on a thermo-analyzer instrument (NETZSCH TG 209F1) combined with an infrared spectrometer (Nicolet IS50, USA).

3. Results and discussion

3.1. Characterization of RuL_3

Because of the strong electrophilic effect of sulfonic ester, the RuL_3 (based on sulfonic ester group) is specially employed to coordinate with few-layers BP. Fig. 2(a) shows the ^{1}H NMR spectrum of RuL_3, a sharp peak at 2.37 ppm corresponds to hydrogen of the $–CH_3$ group, and the two peaks at 7.25 and 7.72 ppm are ascribed to the hydrogen from the benzyl group. By means of the ^{13}C NMR spectra in Fig. 2(b), the synthesis of RuL_3 was successfully confirmed. The peak at 19.93 ppm is associated with carbon from $–CH_3$ group and those at 125.61, 128.52, 140.68 and 141.33 ppm are attributed to carbon atoms from the benzyl group [27]. The same evidence can also be obtained from the infrared spectrum in Fig. 2(c), the two curves have flattened absorption peaks at 3300–3400 cm^{-1} due to the hydroxyl groups in the association water. Compared to the infrared spectrum of $Ru(CH_3COO)_3$, there are several new peaks in the spectrum of RuL_3. The peak at 1600 cm^{-1} corresponds to the stretching vibration of C=C group from benzene structure. The typical peaks at 1220 and 1120 cm^{-1} are associated with the stretching vibration of $-SO_3$. The typical vibration absorption of C–H in aromatics can be found at peak of 810 cm^{-1}, and all the peaks indicate a ruthenium complex based on p-toluenesulfonate is successfully synthesized.

3.2. Micro-structure of BP and its coordination

To unveil the exfoliated effect of BP and its coordination, a series of characterizations are applied in this work. The stripped morphology of BP is characterized by SEM, TEM and AFM. The SEM image (Fig. S1) shows the exfoliated BP is thinner and smaller than the BP crystals which have a multilayer structure with inhomogeneous size [35]. In Fig. 3(a), the TEM image indicates the stripped BP from BP crystals has few-layer structure with a width of several micrometers. Fig. 3(b) shows the high-resolution TEM (HRTEM) image of BP, the lattice fringes of 0.21 nm corresponds to the (0 1 4) plane of BP [18,36], which is consistent with the results of XRD analysis. The typical crystalline structure of the exfoliated BP can be found by the selected-area electron diffraction from Fig. 3(c). Fig. 3(d) exhibits a good dispersibility of RuL_3@BP under transmission electron microscope. An enlarged view of BP from AFM image and the corresponding height profiles are shown in Fig. 3(e) and (f). The stripped BP has a thinner surface with a relative average thickness of 0.53 nm, 1.06 nm and 1.15 nm. Generally, the thickness of a monolayer phosphorene is considered as 0.53 nm [18,27,35,36]. Thereby, the thickness of 0.53 nm and 1.06 nm obtained from Fig. 3(f) is assigned to one to two layers of p atoms, which indicates that the thinner BP nanosheets has been smoothly prepared.

The elements' content and distribution of RuL_3@BP are characterized by the energy dispersive spectrometer (EDS) in Fig. 4. Fig. 4(a) shows the BP nanosheet coordinated by RuL_3 presents as a sphere with several tens of micrometers in diameter, and its edge is rough with a layered structure, which is due to the coordination effect of RuL_3 on the surface of BP. The element contents of carbon (C), oxygen (O), phosphorus (P), sulfur (S) and ruthenium (Ru) are displayed in Fig. 4(b-d). S and Ru element appear in the BP nanosheet identify the successful formation of RuL_3@BP. Fig. 4(e-i) are the elemental mapping images of C, O, P, S and Ru, which proves that there is mainly surface coordination effect between RuL_3 and BP.

Degree of crystallization for BP and RuL_3@BP is characterized by the X-ray powder diffraction (XRD) as shown in Fig. 5(a). For pure BP, three intense diffraction peaks located at 16.7°, 34.1° and 52.2° correspond to the (0 2 0), (0 4 0) and (0 6 0) layered planes of BP and the other four weak peaks located at 26.4°, 34.8°, 55.8° and 56.7° are ascribed to the (0 2 1), (1 1 1), (1 5 1) and (0 6 0) crystal planes of BP [27,35,37]. For RuL_3@BP, its peaks are obviously weaker than that of pure BP, because RuL_3 is coordinated on the surface of BP, which plays an encapsulated effect for BP. The Raman spectra is also employed to characterize the structural integrity of BP and RuL_3@BP. Fig. 5(b) exhibits the representative peaks of A_g^1 (362.1 cm^{-1}), B_{2g} (439.3 cm^{-1}) and A_g^2 (468.1 cm^{-1}), which is attributed to the three characteristic vibrational modes of BP [12,27]. The same peaks also arise in RuL_3@BP sample, which reveals that coordination of RuL_3 does not affect its intrinsic vibration structure. Thermogravimetric analysis (TGA) is conducted under nitrogen to measure the thermal stability of BP and RuL_3@BP. In Fig. 5(c), BP nanosheets exhibit one thermal

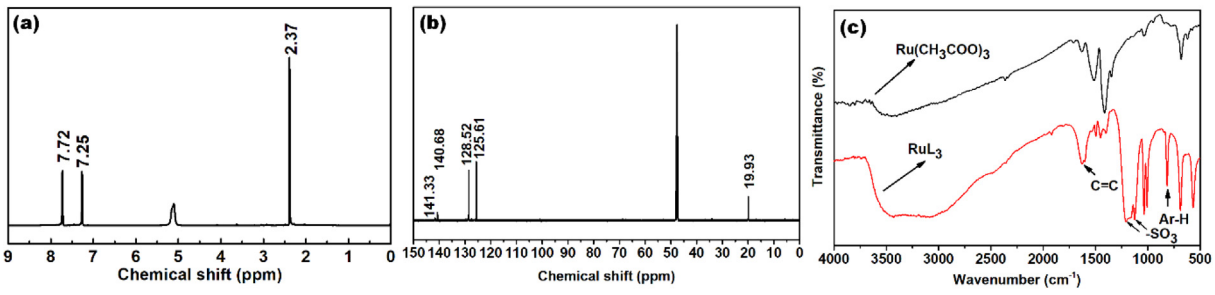

Fig. 2. Characterization of RuL_3: (a) ^{1}H NMR spectra of RuL_3; (b) ^{1}C NMR spectra of RuL_3; (c) FT-IR spectra of $Ru(CH_3COO)_3$ and RuL_3.

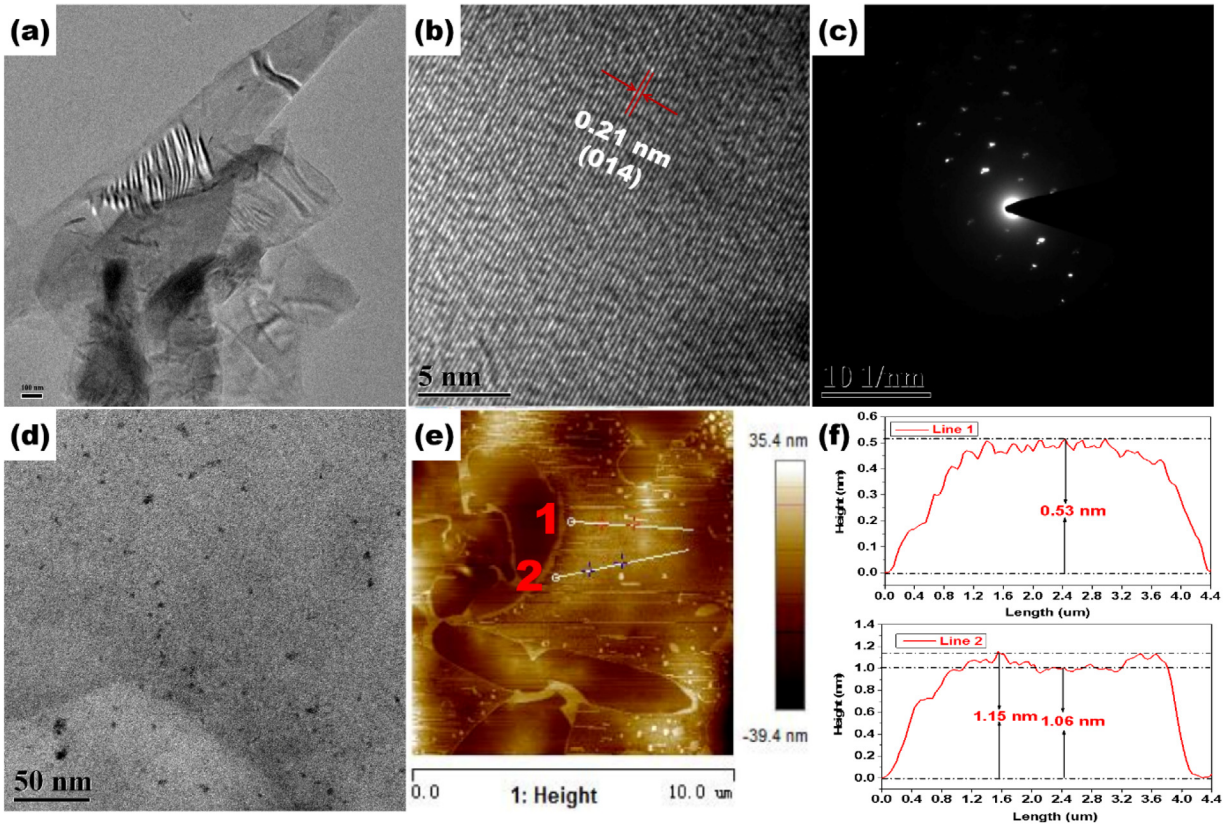

Fig. 3. (a) TEM image of BP nanosheets; (b) HRTEM image of BP nanosheets; (c) SAED pattern of BP nanosheets; (d) TEM image of RuL_3@BP; (e) AFM image of few-layer BP nanosheets; (f) the corresponding height for line 1 and line 2.

decomposition stage between 450 and 550 °C, which is due to the cleavage of the P-P bond, and RuL_3 has a one-step thermal decomposition process between 250 and 350 °C due to the thermal decomposition of p-toluenesulfonic acid groups. However, RuL_3@BP shows two-step mass loss process from 30 to 800 °C. The first degradation step appears in the range of 280–330 °C, due to the thermal decomposition of RuL_3 (about 30% mass loss). After that, the second step occurs between 460 and 540 °C, which is assigned to the thermal decomposition of BP. Meanwhile, Fig. 5(c) indicates RuL_3@BP has a residue of 73.55% after the first stage of thermal degradation and the residue after the second degradation stage is 31.95%. Therefore, the load ratio of RuL_3 on BP is 1:1.57 by a mathematical calculation. From Fig. 5(d), the derivative thermogravimetric analysis (DTG) shows RuL_3 has a higher maximum mass loss rates than that of BP and RuL_3@BP corresponding to the poor thermal stability of p-toluenesulfonate. In addition, the maximum decomposition temperature of RuL_3@BP has a slight shift to high temperature, which is ascribed to the superior heat-resistance of BP.

X-ray photoelectron spectroscopy (XPS) is employed to further probe the surface chemical structure of pure BP and RuL_3@BP. The survey spectrum of pure BP and RuL_3@BP are shown in Fig. 6 (a), the element of O and C appear in the survey spectra of pure BP, which is ascribed to the atmospheric contamination and partial oxidation of BP. Compared with the spectra of pure BP, the content of O element for RuL_3@BP is increased by 5.76 times, and the atomic ratio of O/P enhances from 0.06 (BP) to 1.93 (RuL_3@BP) (Table S1), which is due to the coordination of P-toluenesulfonate on BP. In addition, the new element of Ru arises in the spectra of RuL_3@BP, which demonstrates the BP is successfully coordinated by RuL_3. From Fig. 6(b), P 2p signal of pure BP is divided into three peaks at 129.7, 130.6, and 134.0 eV corresponding to the binding energy of P $2P_{3/2}$ and P $2P_{1/2}$ in P-P bonds and P-O bonds, respectively [35,38]. The P-O bonds is attributed to surface oxidation of BP because BP is unavoidably oxidized during the experimental operation [2,39]. This result is according with the O 1 s survey spectra of pure BP in Fig. 6(a). For RuL_3@BP, its P 2P peaks are shown in Fig. 6(c). The signal is divided into two peaks at 132.6 eV and 134.0 eV, which is ascribed to P-Ru and P-O bonds, respectively. The formation of P-Ru bonds indicates a credible surface coordination between BP and RuL_3, the same analysis is also verified by Ru 3p spectrum from Fig. 6(d). Three obvious peaks located at 462.8, 464.4 and 486.9 eV are associated with P-Ru, Ru $3p_{1/2}$ and Ru $3p_{3/2}$ bonds, respectively, revealing the few-layer BP has been functionalized by RuL_3 and the RuL_3 is preferred to coordinate on the surface of BP, which is consistent with the results of EDS analysis (Fig. 4) and XRD analysis (Fig. 5(a)).

3.3. Stability of BP and RuL_3@BP

It is well known that the poor stability of BP in air and water restricts its application in many fields. Therefore, it is crucial to enhance the stability for the application of BP. To assess the effect of surface coordination on the stability of BP, the RuL_3@BP and pure BP were firstly exposed to natural environment for different time, and then dispersed in water with a same concentration of 30 ppm. The photos of the dispersion after standing for 1 h are shown in Fig. 7(a). Obviously, the dispersion of RuL_3@BP almost has no change after 8 days but the pure BP dispersion becomes transparent with partial sediments in the bottom. A UV 2550 spectrometer is conducted to test the optical absorbance of BP and RuL_3@BP in water in Fig. 7(b) and (c). Fig. 7(b) shows the pure BP has an obvious decrease at the absorbance intensity with the exposure time in environment. After 8 days, the pure BP decreases by 85% in the absorbance at 450 nm (A) compared with the initial value (A_0). Now it has been confirmed that BP is easy to form P_xO_y with the effect of oxygen and the water will accelerate the

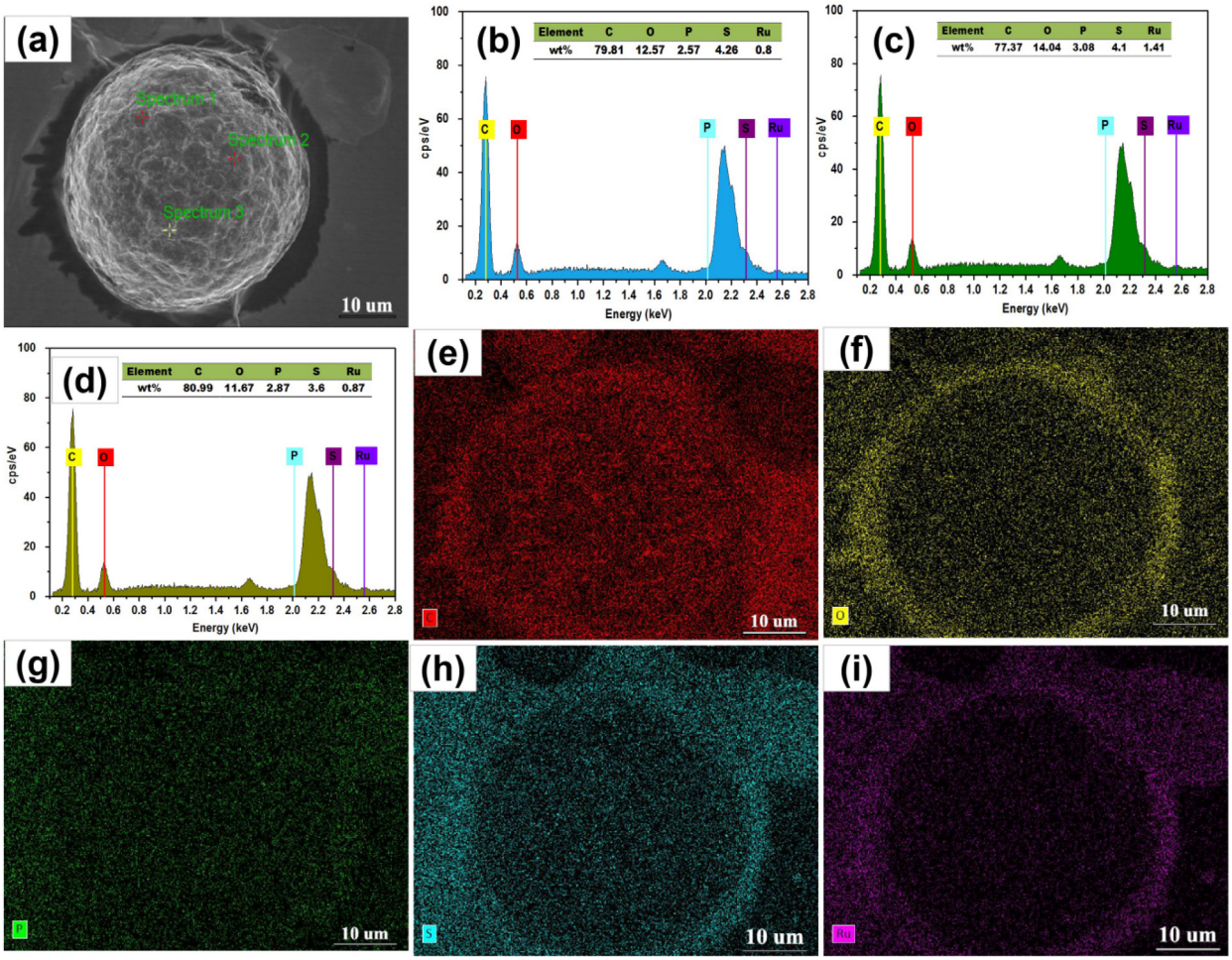

Fig. 4. EDS analysis of RuL_3@BP: (a) SEM image of RuL_3@BP; (b), (c), (d) distribution diagram of element from the spectrums in (a); mapping image of (e) carbon (C), (f) oxygen (O), (g) phosphorus (P), (h) sulfur (S) and (i) ruthenium (Ru).

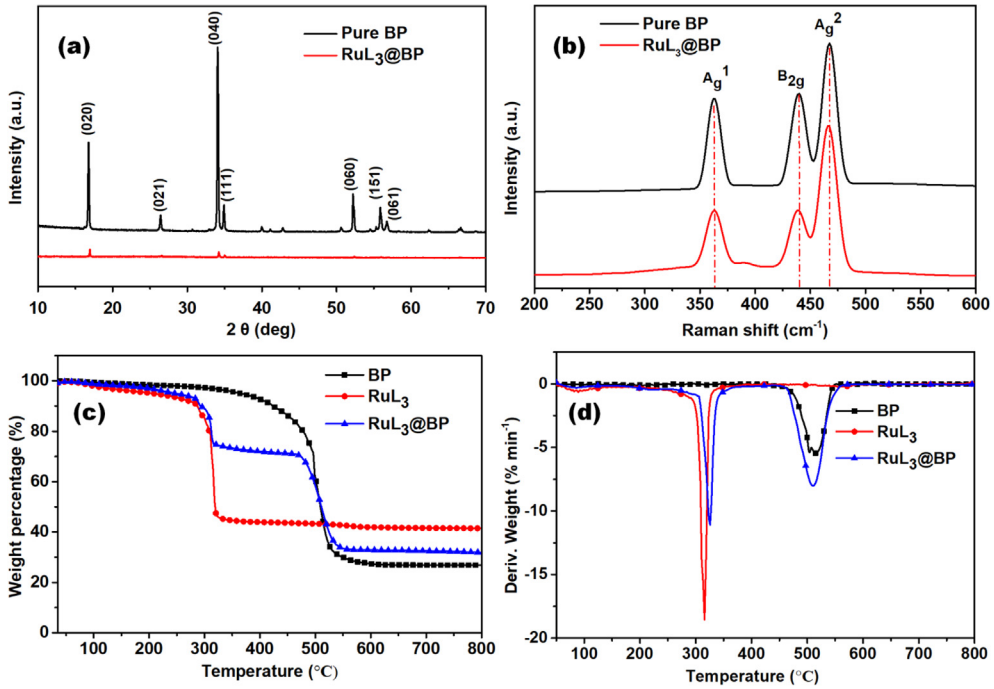

Fig. 5. (a) XRD patterns of pure BP and RuL_3@BP; (b) Raman spectra of pure BP and RuL_3@BP; (c) TGA curves of BP, RuL_3 and RuL_3@BP; (d) DTG curves of BP, RuL_3 and RuL_3@BP.

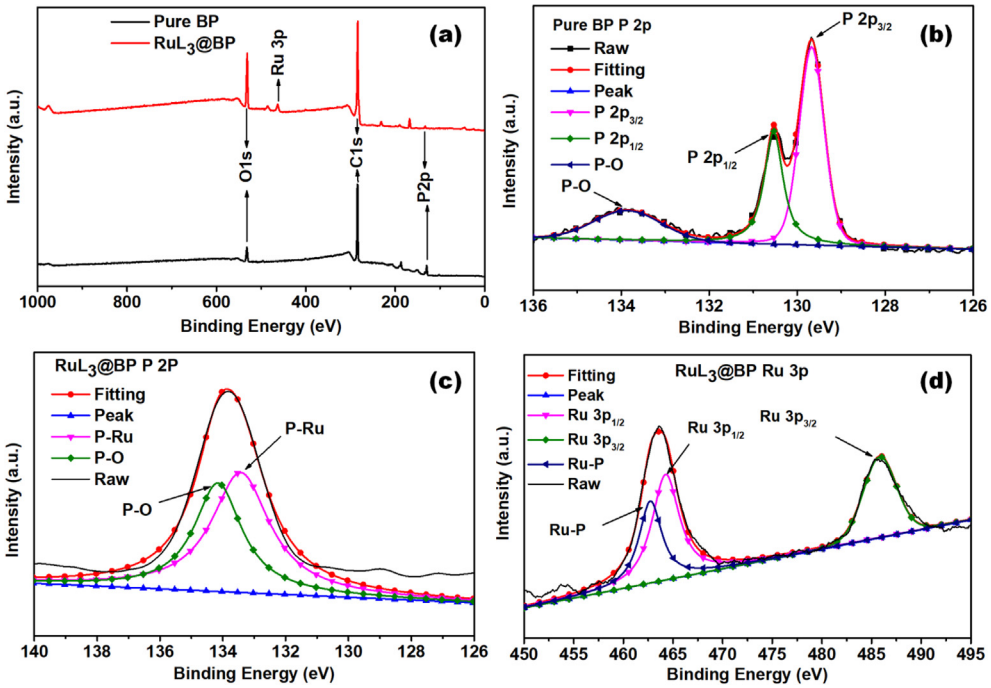

Fig. 6. (a) XPS survey spectra of pure BP and RuL_3@BP; (b) high-resolution P 2p spectra of pure BP; (c) high-resolution P 2p spectra of RuL_3@BP; (d) high-resolution Ru 3p spectra of RuL_3@BP.

transformation of P_xO_y to PO_4^{3-} [27]. It will result in a quick degradation of BP, leading to a reduced optical absorbance. Compared to pure BP, the RuL_3@BP is also dispersed in water and its absorbance changes are shown in Fig. 7(c). The absorbance intensity of RuL_3@BP at 450 nm only decreases by 18% from the original value, informing the RuL_3@BP is more stable than pure BP in natural environment. In Fig. 7(d), supplementary experiments demonstrate that RuL_3@BP has favorable stability in ethanol and N, N-dimethylformamide (DMF). This improvement of stability for BP is of great significance for its practical application.

3.4. Dispersibility of BP and RuL_3@BP in EP

For a long time, the comprehensive properties of composite materials have been affected by the dispersion of nanofillers in substrates [40]. As a typical two-dimensional inorganic nano-filler, the direct incorporation of BP into polymer will lead to agglomeration, which seriously restricts its application. Therefore, improving the dispersion of BP in the resin is the basis for enhancing other properties and has important research significance [35]. The optical microscope and SEM are used to observe the dispersion state of BP and RuL_3@BP in epoxy with a

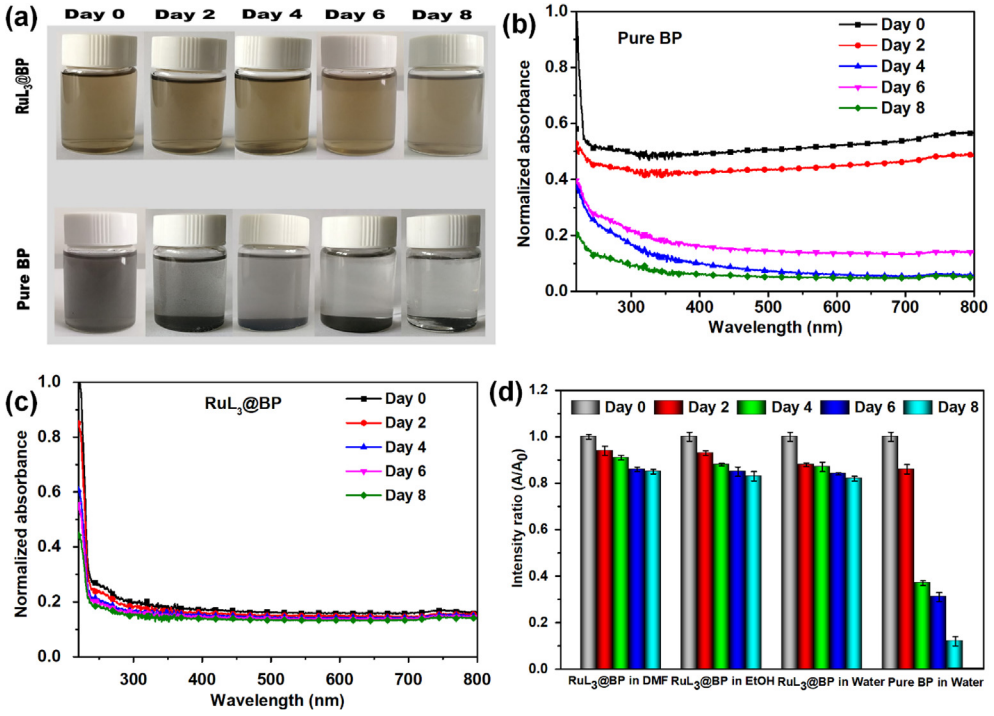

Fig. 7. Stability assessment of pure BP and RuL_3@BP under ambient conditions: (a) digital photos; (b) absorption spectra of pure BP and (c) RuL_3@BP dispersed in water after exposure to air for different time; (d) variation of the absorption at 450 nm (A/A_0) of pure BP and RuL_3@BP dispersed in DMF, EtOH and water after exposure in natural environment for different time.

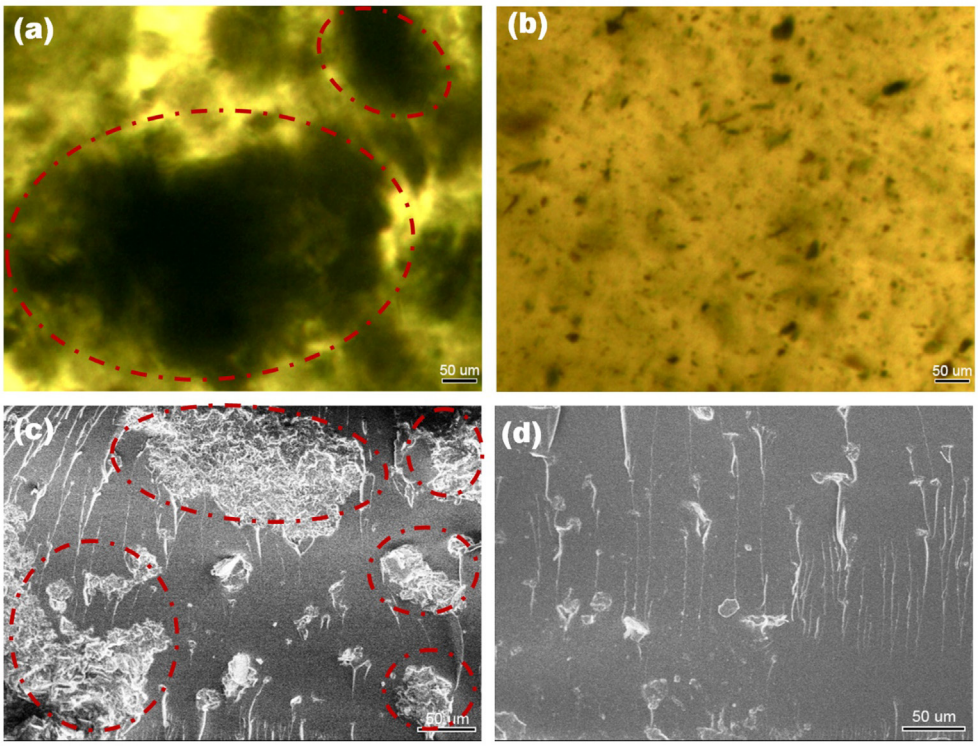

Fig. 8. The photos under optical microscope: (a) pure BP 3.0 in epoxy; (b) RuL_3@BP 3.0 in epoxy; SEM photos: (c) BP 3.0 in epoxy; (d) RuL_3@BP 3.0 in epoxy.

same loading of 3.0 wt% as shown in Fig. 8. Fig. 8(a) clearly and intuitively shows that 3.0 wt% BP is heavily agglomerated in EP resin, while the composites with the incorporation of RuL_3@BP 3.0 are dispersed uniformly in Fig. 8(b). The same strong evidence can be found from the SEM of fracture surface in Fig. 8(c) and (d). Obviously, BP is largely re-aggregated in the composites from Fig. 8(c). For EP/RuL_3@BP 3.0, smooth and ordered freeze-fractured surface can be clearly found in Fig. 8(d), which demonstrates that the coordination of BP by RuL_3 can dramatically improve the interfacial compatibility, thus enhances the dispersion of RuL_3@BP in epoxy. Due to the van der Waals force between the layers, the inorganic nanomaterials are easily re-aggregated in the polymer resin. Surface modification can effectively improve the dispersibility, but with the increase of the added amount, the dispersibility tends to gradually deteriorate, so low-content, high-efficiency nanofillers are the development direction of polymer nanocomposites.

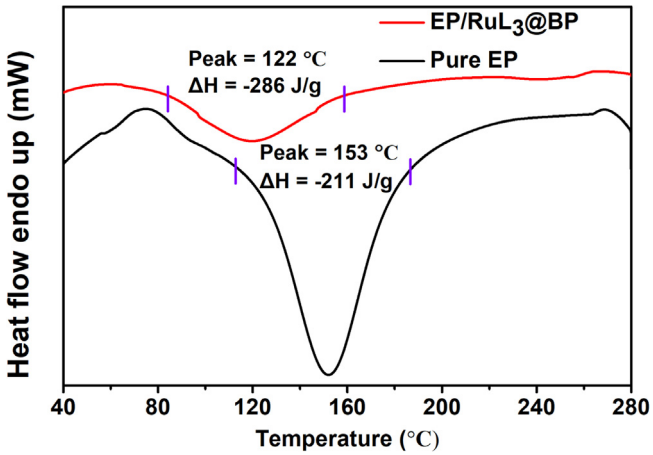

Fig. 9. DSC thermograms of EP and EP/RuL_3@BP 3.0.

3.5. Catalytic effect of RuL_3@BP

Because ruthenium compounds are often used as catalysts for various reactions, such as ammonia synthesis, hydrogenation, isomerization, etc., it is necessary to study the catalytic effect of RuL_3@BP on the curing of epoxy. Differential scanning calorimetry (DSC) is employed to measure the curing process of pure EP and EP/RuL_3@BP 3.0 in Fig. 9. The exothermic peak temperature of pure EP is as high as 153 °C and its exothermic enthalpy is 211 J g^{-1}, which is ascribed to the uncatalyzed reaction of pure EP. Compared with pure EP, both the exothermic peak temperature and exothermic enthalpy of EP/RuL_3@BP 3.0 has an obvious change. The exothermic peak temperature of EP/RuL_3@BP 3.0 has reduced to 122 °C and its exothermic enthalpy increases to 286 J g^{-1}. This result demonstrates that RuL_3@BP has a significant catalytic effect for the curing of EP. This phenomenon may be attributed to the metal vacancies of ruthenium atoms, which attracts hydrogen-containing groups in the reaction, causing uneven distribution of the electron cloud, resulting in a decrease in the activation energy of the curing reaction, so that the reaction can be carried out at a lower temperature [41].

3.6. Tensile strength and thermal stability for EP nano-composites

Tensile strength is used to assess the mechanical properties of EP composites. As shown in Fig. 10(a), the tensile strength of pure EP is 73.5 Mpa at normal temperature, but the tensile strength of EP/BP 3.0 has dropped to 70.1 Mpa at the same temperature, which is due to the serious agglomeration of BP in EP resin. The agglomeration of BP may reduce the crosslink density of the curing system, which causes a slight decrease in the tensile strength. For EP/RuL_3@BP nanocomposites, with the amount of RuL_3@BP increases from 1.0 to 3.0 wt%, the tensile strength of EP/RuL_3@BP nanocomposites increases by 6.73%, 13.61% and 20.95%, respectively. The increased tensile strength is primarily ascribed to the enhanced compatibility of RuL_3@BP in EP. On the other hand, RuL_3@BP has an obvious catalytic effect for the curing of epoxy, which will improve the crosslink density of the whole system. This

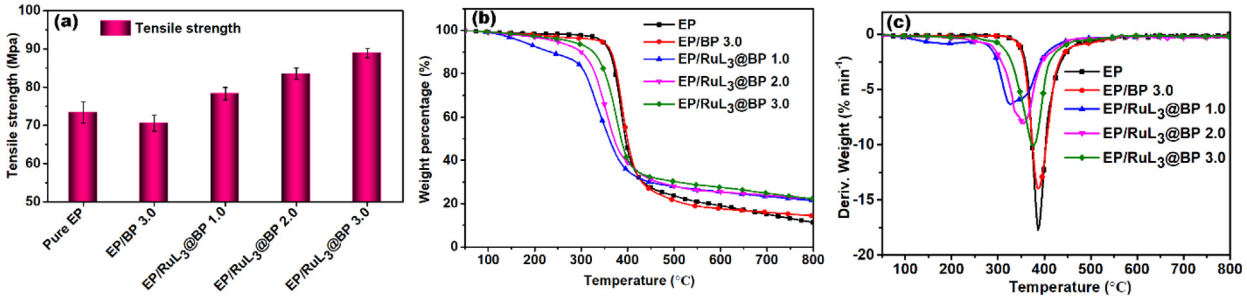

Fig. 10. (a) Tensile strength; (b) TGA and (c) DTG of EP and its nanocomposites incorporated with different RuL_3@BP contents.

result is consistent with Fig. 8 and Fig. 9. TGA is conducted to measure the heat-resistance of samples, the detail data are listed in Table S2. Fig. 10(b) exhibits that all the EP/RuL_3@BP and EP/BP 3.0 have similar pyrolysis behavior as pure EP, which occurs at 200–500 °C by a one-step mass loss process. The initial degradation temperature of the EP/RuL_3@BP nanocomposites decreased slightly, which is due to unreacted p-toluenesulfonic acid functional group. However, when the content of RuL_3@BP is increased, an obvious improvement can be seen in initial degradation temperature, which is ascribed to high thermal stability of BP. Compared with neat EP, with increasing RuL_3@BP content from 1.0 to 3.0 wt%, the residual char rate for EP/RuL_3@BP are improved by 89.69–96.83%. However, for the EP/BP 3.0 nanocomposite, it only has a char yield of 14.44% at 800 °C, which is far lower than the char residue (22.34%) of EP/RuL_3@BP, indicating that the coordination of BP by RuL_3 can accelerate the formation of residual char. In fact, both BP and sulfonate have the function of catalyzing char formation, thus improving the content of char residues. In Fig. 10(c), the derivative thermogravimetric analysis (DTG) indicates the largest mass loss rate for nanocomposites are exceedingly smaller than that of pure epoxy. Which is attributed to the stable puckered structure of BP, restricting the penetration of oxygen and inflammable gases, and RuL_3 will facilitate the charring formation, thereby enhancing the thermal stability of EP nanocomposites [35].

3.7. Flame retardancy of EP composites

The fire performance of EP nanocomposites is investigated in Fig. 11. The limiting oxygen index (LOI) is employed to evaluate the least oxygen concentration required for the combustion of the polymer, which can be used to quantitatively evaluate the fire performance [42,43], whereas the UL-94 test can more intuitively reflect the true combustion process of the material [44–46]. As shown in Fig. 11(a), the LOI value of pure EP is only 24.7% and its UL-94 test exhibits no rating (NR), while the LOI value for EP/RuL_3@BP are notably enhanced by 12.55–26.72% with the incorporation of RuL_3@BP content from 1.0 to 3.0 wt%. Particularly note is that the LOI value of EP/RuL_3@BP 3.0 enhances to 31.3%, and the sample can easily pass UL-94 V-0 combustion rating. However, the LOI value of EP/BP 3.0 is only 29.8% and it just passes the UL-94 V-1 rating. This indicates that BP can do improve the flame retardancy, but the direct addition of BP will lead to a poor dispersion, which has an adverse effect on the fire performance [47]. BP coordinated by RuL_3 can dramatically enhance the dispersion of BP in polymer, and improve the flame-retardant efficiency of BP, so both the LOI value and UL-94 test of EP nanocomposites are raised [7]. The detailed data are shown in Table S3. When leaving the ignition, the neat EP burnt fiercely, but the EP/BP 3.0 and EP/RuL_3@BP 3.0 nanocomposite can self-extinguish at 24 s and 3 s, respectively. It can be surmised that the introduction of BP and RuL_3@BP will promote the char formation with higher heat-resistance, which can restrict the contact of flammable gases and improve the flame-retardant efficiency. The cone calorimeter is regarded as an efficient, low-cost tool for determining and predicting the fire performance of materials, and can obtain a large amount of data on flame retardant performance. The detailed data are exhibited in Table S4 in the Supporting Information.

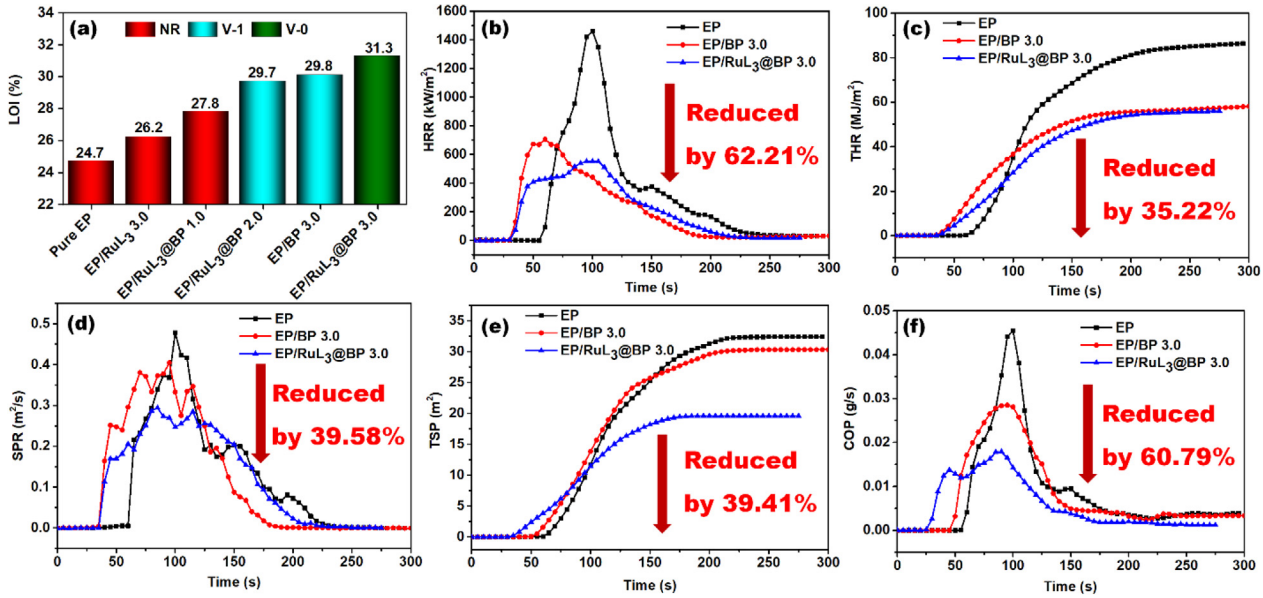

Fig. 11. (a) LOI values and the UL-94 vertical test; (b) HRR and (c)THR curves of EP, EP/BP 3.0 and EP/RuL_3@BP 3.0; (d) SPR and (e) TSP versus time curves of EP, EP/BP 3.0 and EP/RuL_3@BP 3.0; (f) COP versus time curves of EP, EP/BP 3.0 and EP/RuL_3@BP 3.0.

Table 1
The Filler Efficiency of Previous Literature and that of Our Work.

Filler	Fraction (wt%)	φ_{PHRR}	φ_{THR}	φ_{SPR}	φ_{TSP}	φ_{LOI}	Matrix	Ref.
MP-PEPA	39.75	2.01%				0.38%	PP	[49]
MCU@APP	30.0	1.75%				3.34%	PP	[50]
GO/SEP/BA	23.0	1.10%				2.37%	Cellulose nanofibers	[45]
CH/APP/CH/PAA-KAO	17.8	3.75%	2.23%		3.33%		PUF	[46]
PD-LDH@MF	15.0	4.60%	1.64%			3.24%	EVA	[51]
APP/PEI	13.8	4.88%	3.27%			0.90%	Ramie fabrics	[52]
MH-APP	13.7					3.37%	PU	[43]
Ionic liquid-based metal–organic hybrid	6.0	5.16%	0.17%	3.85%	2.56%		EP	[48]
Frs@rGO	5.0	7.01%				8.11%	EP	[53]
g-C_3N_4/OAHPi hybrids	4.0	6.93%	2.39%	5.47%			PS	[54]
1-vinyl-3-(diethoxyphosphoryl)-propylimidazolium bromide	4.0	16.25%	3.52%			8.48%	EP	[42]
BP/G	3.55	13.56%	10.88%				WPU	[34]
Fr@PZS	3.0	15.34%	9.03%				EP	[55]
BP@EC/Exf	3.0	14.84%	11.50%				PUA	[7]
FGO	2.0	18.00%	6.89%				PS	[56]
RuL_3@BP	3.0	20.74%	11.74%	13.19%	13.14%	8.91%	EP	This work

The heat release rate (HRR) and the total heat release (THR) are generally considered to be the important indicators for evaluating the flame retardancy [7,35]. Fig. 11(b) shows the HRR curves of pure EP and its nanocomposites. It is obvious that EP has a very high peak heat release rate (PHRR) of 1461 kW m^{-2}, whereas incorporating only 3.0 wt% RuL_3@BP into EP, the PHRR of EP/RuL_3@BP 3.0 sample decreases dramatically to 552 kW m^{-2}, which is reduced by 62.21%. As a control experiment, the HRR of EP/BP 3.0 sample is also measured. The PHRR of EP/BP 3.0 is 705 kW m^{-2}, which is smaller than that of EP but larger than that of EP/RuL_3@BP 3.0. The THR curves are shown in Fig. 11(c). Similar to the HRR, The THR of pure EP is as high as 86.36 MJ m^2. By adding BP and RuL_3@BP at content of 3.0 wt%, the THR of EP/BP 3.0 and EP/RuL_3@BP 3.0 decrease directly to 58.38 MJ m^2 and 55.94 MJ m^2, respectively. Especially for EP/RuL_3@BP 3.0, its THR is reduced by 35.22%. All above results verify that the incorporation of RuL_3@BP 3.0 in EP matrix can significantly inhibit the peak heat release rate and the total heat release of EP/RuL_3@BP nanocomposites in the combustion, revealing the remarkable flame retardancy of RuL_3@BP. In addition, the fire risk of EP nanocomposites is also evaluated by the fire growth rate (FIGRA) [48]. The formula of FIGRA is expressed as follows:

$$FIGRA = \frac{PHRR}{tPHRR} \quad (1)$$

Based on Table S4 and the formula (1), the pure EP has a high FIGRA of 14.61 kW m^{-2} s^{-1}, whereas the FIGRA of EP/BP 3.0 nanocomposite is 11.75 kW m^{-2} s^{-1}. Especially, the FIGRA of EP/RuL_3@BP 3.0 nanocomposites decreases by 62.22% (5.52 kW m^{-2} s^{-1}) compared with that of neat EP, which confirms that the FIGRA has been significantly decreased by the introduction of RuL_3@BP in epoxy, owing to the excellent flame-retardant performance of RuL_3@BP. The smokes emitted by the combustion of the polymer are particularly hazardous and must be considered in the flame retardant. Meanwhile, the smoke production rate (SPR), total smoke production (TSP) and the amount of CO produced per second (COP) are employed to assess the smoke suppression effect of EP nanocomposites in Fig. 11(d), (e) and (f). As can be seen from Fig. 11(d), the pure EP has an intense peak SPR of 0.48 m^2 s, the sample of EP/BP 3.0 shows a lower value of 0.40 m^2 s, while the peak SPR of EP/RuL_3@BP 3.0 nanocomposites decreases by 39.58% (0.29 m^2 s) compared with that of pure EP, indicating the addition of RuL_3@BP can effectively reduce the smoke production rate. Fig. 11 (e) presents the TSP of EP/RuL_3@BP 3.0 nanocomposites is only 19.60 m^2, with a reduction of 39.41% compared to that of pure EP (32.35 m^2), which is due to the synergetic catalytic charring effect between RuL_3 and BP nanosheets, thereby inhibiting the diffusion of flammable gas and isolating the unburned materials from contacting with the fire source during combustion. CO is the main toxic and harmful gas released in the combustion of polymers, which will cause a serious damage to the environment. The COP of samples are revealed in Fig. 11 (f), pure EP has a higher peak COP of 0.045 g s^{-1} and the peak of EP/BP 3.0 is 0.028 g s^{-1}, whereas the peak COP of EP/RuL_3@BP 3.0 is only 0.018 g s^{-1}, which leads to a 60.79% decrease compared with that of pure EP. All the curves from Fig. 11 (b)-(f) show that the EP composite incorporated with BP and RuL_3@BP is more prone to pyrolyze in the initial stage of combustion, which may be due to the decomposition of p-toluenesulfonate and the rapid heat transfer efficiency of RuL_3@BP, the evidence can be found in Fig. 16. Meanwhile, RuL_3 functionalized BP mainly occurs on the surface of BP, and the benzenesulfonic acid group has poor heat resistance, so its pyrolysis will occur earlier than EP resin in the early stage of combustion. These results obtained from the cone calorimetry confirm that the addition of RuL_3@BP can not only effectively form dense char residues, but also significantly inhibit the generation of smoke.

Filler efficiency can be used to evaluate the contribution of filler to composites properties at a unit weight, the higher the efficiency, the better the performance for the filler [57]. The filler efficiency for PHRR, THR, SPR and TSP are evaluated by its decreased rate defined as $\varphi_{PHRR} = \frac{PHRRm - PHRR}{PHRRm \times wt\%}$, $\varphi_{THR} = \frac{THRm - THR}{THRm \times wt\%}$, $\varphi_{SPR} = \frac{SPRm - SPR}{SPRm \times wt\%}$, $\varphi_{TSP} = \frac{TSPm - TSP}{TSPm \times wt\%}$, where *PHRRm*, *THRm*, *SPRm* and *TSPm* are the peak heat release rate, total heat release, smoke production rate and total smoke production for the matrix material, respectively. The *PHRR*, *THR*, *SPR* and *TSP* are the corresponding values for composites and *wt*% is the mass fraction of added filler. The filler efficiency for LOI is assessed by the increased rate(φ_{LOI}), which is defined as $\varphi_{LOI} = \frac{LOI - LOIm}{LOIm \times wt\%}$, *LOI* is the LOI value for the composites, *LOIm* is the LOI value for the substrates and *wt*% is the mass fraction of added filler. Table 1 lists some previous results on the filler efficiency to compare our findings with previous studies. The data indicates the filler efficiency in our work is indeed remarkable, which demonstrates a quite high flame-retardant efficiency can be obtained by introducing a lower content of RuL_3@BP into EP.

To further investigate the combustion behavior of EP and its composites, TG-FTIR is conducted to characterize the emissions of volatile gases for EP, EP/BP 3.0 and EP/RuL_3@BP 3.0 nanocomposites. Fig. 12 presents the absorption intensity of the representative products curves for different samples. Some typical peaks for the pyrolysis products are as follows: hydrocarbons (2970 cm^{-1}); carbon dioxide (CO_2) (2350 cm^{-1}); carbon monoxide (CO) (2170 cm^{-1}); carbonyl compounds (1750 cm^{-1}) and aromatic compounds (1510 cm^{-1}) [7,35]. Compared with the pure EP, after adding 3.0 wt% BP and 3.0 wt% RuL_3@BP into EP, all the maximum absorption intensities of representative volatile products, for instance, hydrocarbons, CO_2, CO, carbonyl compounds and aromatic compounds, are dramatically

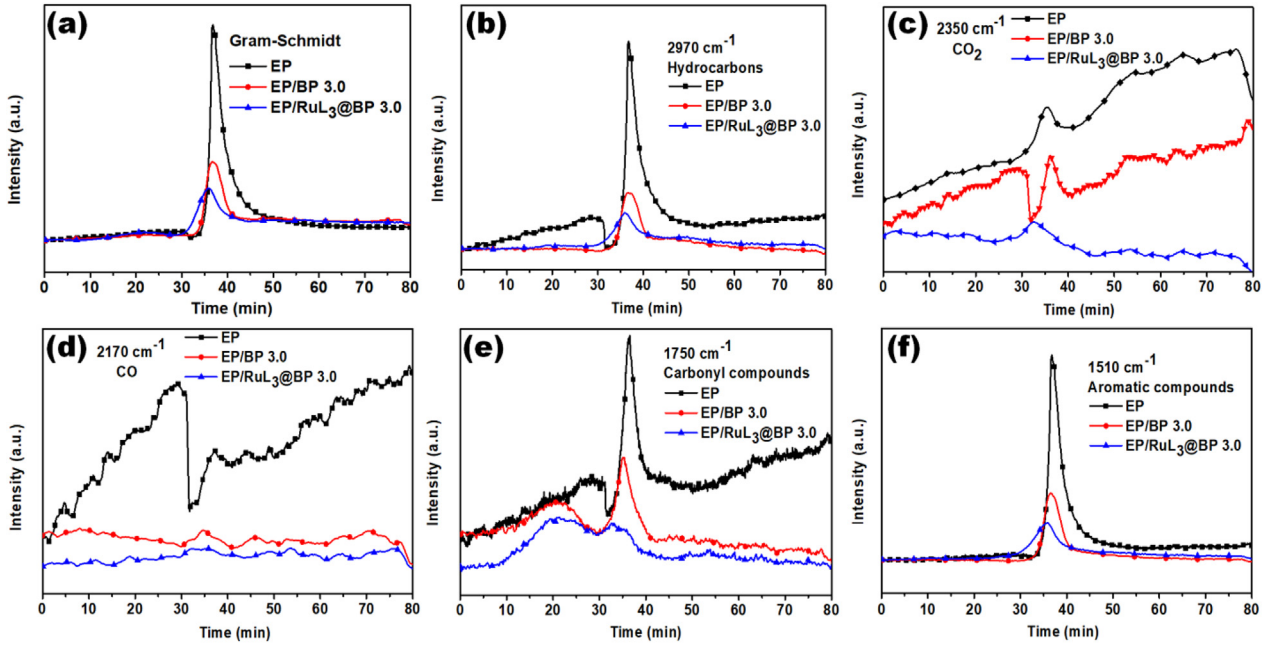

Fig. 12. Absorbance intensity of volatile gas for the samples: (a) total volatile gas; (b) hydrocarbons; (c) carbon dioxide (CO_2); (d) carbon monoxide (CO); (e) carbonyl compounds; (f) aromatic compounds.

decreased. Undoubtedly, EP/RuL_3@BP 3.0 nanocomposites show the smallest absorption intensity in the typical pyrolysis products. This is because the incorporation of RuL_3@BP 3.0 promotes the charring formation in combustion and decreases the volatility of pyrolysis products, which is in compliance with the TGA results. Generally, the main toxic gas from the combustion process of epoxy is recognized as CO. With the increase of pyrolysis time, the CO release of epoxy increases significantly, while the CO release for EP/BP 3.0 and EP/RuL_3@BP 3.0 are very lower. When the heating time is over 75 min, the CO release of EP/RuL_3@BP 3.0 is gradually decreased, which is consistent with the result of COP analysis. The decrease of CO release is favorable for the suppression of smoke toxicity, the results in Fig. 12 are unanimous with the results of cone calorimeter test (Fig. 11), and demonstrating RuL_3@BP can promote a rapid formation of char residue and inhibit the contact of flammable gas with fire zone, thus effectively decreasing the release of pernicious gases.

The char residues obtained from the combustion process can provide an important perspective to investigate reasonable flame-retardant mechanism. The digital photos of char layer from cone test and SEM images of char residue for composites are exhibited in Fig. 13. For the pure EP, there is only a few of residual char in the instrument (Fig. 13(a)). With increasing of the RuL_3@BP content from 2.0 to 3.0 wt %, the amount of the char residues is gradually increasing, and the surface structure is more compact and condense (Fig. 13(b) and (c)). Especially for the sample of EP/RuL_3@BP 3.0 (Fig. 13(c)), its char residues have a highest amount than that of other samples, implying the catalytic charring effect of EP nanocomposites is significantly improved with the enhancement of the RuL_3@BP content. However, the amount of char residues for EP/BP 3.0 is obviously lower than that of EP/RuL_3@BP 3.0, there exists a large hole on the char residue surface (Fig. 13 (d)), which is due to the uneven dispersion of the flame retardant in the EP during the combustion. Fig. 13(e) shows the char residue of EP has a loose surface morphology with some big opening hole. Consistent with the results of digital photos, as the increase of RuL_3@BP content, the SEM image of char residue becomes thicker and smoother (Fig. 13 (f) and (g)). Notably, a quite denser char layer with few of holes is present in EP/RuL_3@BP 3.0 nanocomposites (Fig. 13(g)). Nevertheless, the char residue of EP/BP 3.0 reveals a relatively fluffy structure with a few of microspores (Fig. 13(h)). As considered in the EP/RuL_3@BP 3.0 sample, the continuous, compact and dense char residues are formed due to the higher heat-resistance of BP and the synergetic catalytic charring effect between BP and RuL_3. The formation of the dense char residue will hinder further combustion of the polymer, restricting the release of heat and diffusion of inflammable gases [42]. The carbonization degree of char residues is an important index for combustion behavior, a higher carbonization degree is more favorable to form an effective barrier to forbid the internal materials ignition. The Raman spectroscopy is utilized to characterize the graphitization degree of char layer. The Raman spectra of residual char are shown in Fig. 13(i-k), two characteristic peaks at 1348 cm^{-1} and 1588 cm^{-1} are determined as D and G peak. In prior studies, the area ratio for D peak to G peak (I_D/I_G) was employed to assess the graphitization degree and a smaller I_D/I_G represented a lager graphitization degree. Specifically, the I_D/I_G for pure EP is 5.10 (Fig. 13(i)), and the EP/BP 3.0 presents an I_D/I_G of 3.93 (Fig. 13(j)), whereas the EP/RuL_3@BP 3.0 exhibits a lower I_D/I_G (3.52) in Fig. 13(k), indicating a high carbonization degree. These consequences are attributed to the cooperative catalytic charring from both BP nanosheets and RuL_3 in EP nanocomposites during the combustion.

The FT-IR spectra of the residual char for EP and its nanocomposites after cone tests are displayed in Fig. 14(a), the peaks located at 1610, 1515, 1440, 1127 and 620 cm^{-1} correspond to the carbonized aromatic structure. Compared with pure EP, two weak peak at 1390 cm^{-1} and 1110 cm^{-1} appear in the residual char for EP/BP and EP/RuL_3@BP nanocomposites, which are ascribed to the stretching modes of O-P=O and P-O-P from the burned BP [34]. In addition, EP/RuL_3@BP nanocomposites also indicate a peak at 997 cm^{-1}, owing to the characteristic absorption of S=O bonds, confirming that there is a coordination between BP and RuL_3. Fig. 14(b) presents the XRD patterns of the charring residues for EP and its nanocomposites after combustion. A broad peak located at 18.5° can be seen from pure EP, which has a crystal plane spacing of 0.4797 nm, indicating the formation of loose charring layer. Compared with the char residue of pure EP, after the addition of BP and RuL_3@BP, the diffraction peaks of char residues gradually move toward the direction of a larger diffraction angle, demonstrating that the inter-planar spacing becomes smaller, confirming the formation of compact and dense char residues, which is completely in accordance with the results of SEM analysis in Fig. 13. Especially for

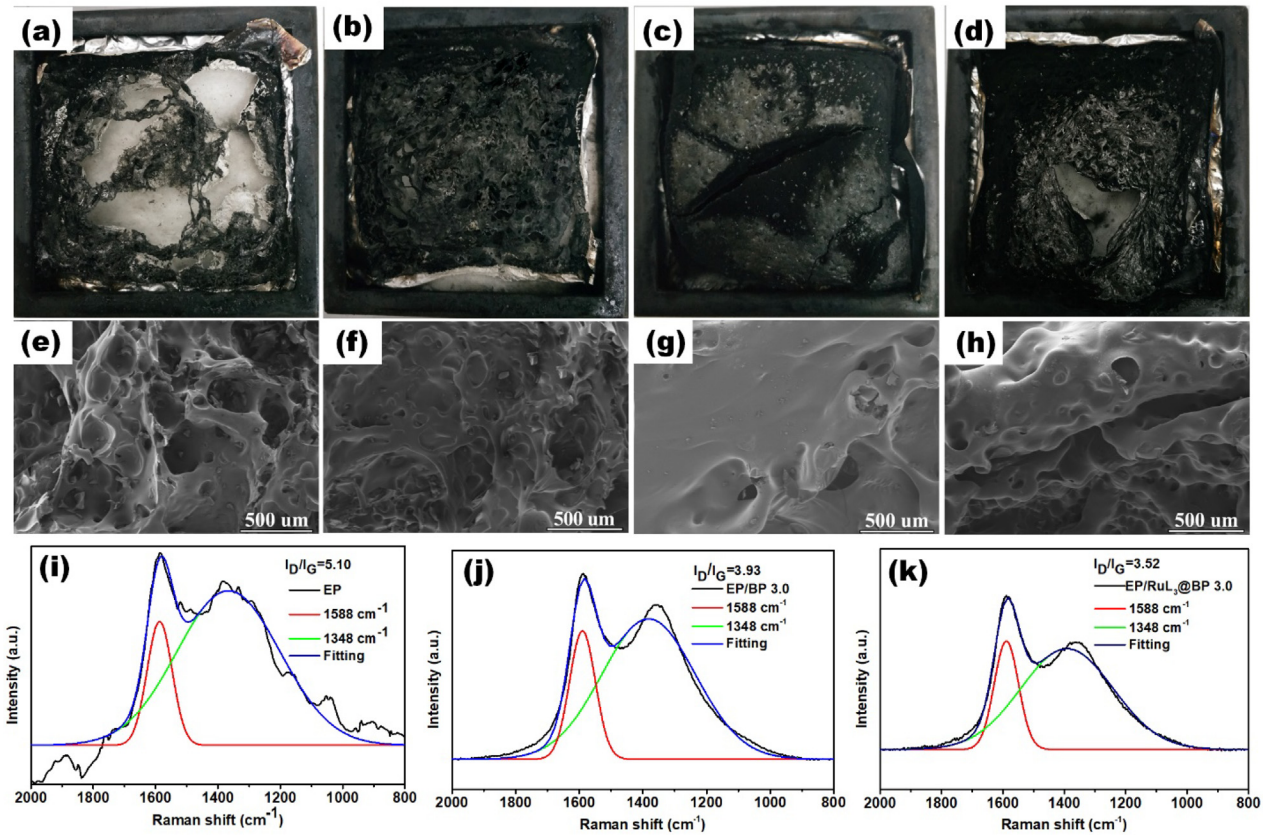

Fig. 13. Digital photos of residual char from top view: (a) pure EP; (b) EP/RuL_3@BP 2.0 nanocomposites; (c) EP/RuL_3@BP 3.0 nanocomposites; (d) EP/BP 3.0 nanocomposites; SEM images of residual char: (e) pure EP; (f) EP/RuL_3@BP 2.0 nanocomposites; (g) EP/RuL_3@BP 3.0 nanocomposites; (h) EP/BP 3.0 nanocomposites; Raman spectra of residual char: (i) pure EP; (j) EP/BP 3.0 nanocomposites; (k) EP/RuL_3@BP 3.0 nanocomposites.

EP/BP 3.0 and EP/RuL_3@BP 3.0 nanocomposites, four peaks located at 17.1°, 26.8°, 34.4° and 52.5° are observed, corresponding to (0 2 0), (0 2 1), (0 4 0) and (0 6 0) crystal planes of BP. This indicates that few of BP nanosheets still exist in the char layer of EP samples after the combustion, which is ascribed to the increased content of BP and RuL_3, leading to poor dispersion of the nanofiller in EP resin and partial agglomeration. Owing to the excellent heat-resistance of BP in the combustion, some BP nanosheets has not been completely pyrolyzed, the results are also consistent with Qiu's work [7]. Fig. 14(c) exhibits the XPS spectra of EP, EP/BP 3.0 and EP/RuL_3@BP 3.0, the elements of C, N and O can be discovered on the surface of all the samples, whereas the P element only appears in the char layer of EP/BP 3.0 and EP/

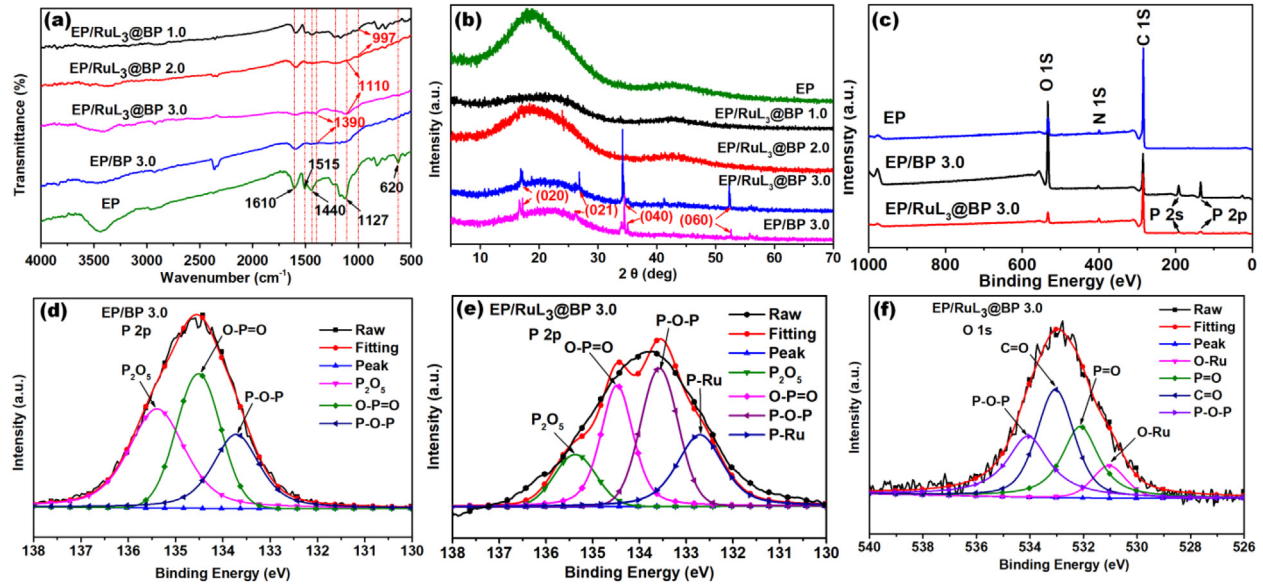

Fig. 14. (a) FT-IR spectrum and (b) XRD patterns of charring; (c) XPS survey spectra for the char residues; high-resolution P 2p XPS spectrum: (d) EP/BP 3.0; (e) EP/RuL_3@BP 3.0; (f) high-resolution O 1 s XPS spectra of EP/RuL_3@BP 3.0.

RuL_3@BP 3.0 nanocomposites, owing to the undecomposed BP and its derivatives, for instance, P_xO_y from the thermal degradation process [58]. The XPS spectrum in P 2p area for EP/BP 3.0 and EP/RuL_3@BP 3.0 are displayed in Fig. 14(d-e). The P 2p peaks of EP/BP 3.0 sample are deconvoluted into three peaks at 133.5, 134.6 and 135.5 eV corresponding to O-P-O, O-P=O and P_2O_5 bonds, respectively [35]. Fig. 14(e) presents the P 2p peaks of EP/RuL_3@BP 3.0 can be divided into four peaks at 132.6, 133.5, 134.6 and 135.5 eV, which are attributed to P-Ru, O-P-O, O-P=O and P_2O_5 bonds, respectively, demonstrating the formation of the oxidative derivatives of BP such as P_xO_y in the combustion [35]. Meanwhile, the existence of P-Ru bonds proves once again that BP nanosheets has been successfully coordinated with RuL_3. The O 1 s XPS spectra of EP/RuL_3@BP 3.0 in Fig. 14(f) also can confirm the above results. There exist several strong peaks corresponding to P=O, C=O and O-P=O bonds, respectively. It is worth noting that a weak peak at 530.4 eV can be observed in the O 1 s XPS spectrum, which is ascribed to the O-Ru bonds, revealing the formation of ruthenium oxide during the combustion of EP/RuL_3@BP 3.0 nanocomposites.

3.8. Flame retardant mechanism

By means of the whole results and analysis, a probable flame-retardant mechanism is proposed in Fig. 15. The combustion process can be subdivided into two stages. In the first burning section (under 450 °C), the p-toluenesulfonate is thermally decomposed to generate sulfur oxides, these sulfur oxides react with the water generated from the combustion of the polymer to form sulfuric acid derivatives, which accelerate the formation of charring residues (Fig. 5 (c) and Fig. 13(c)). Meanwhile, BP nanosheets and ruthenium oxide which is formed from combustion act as barrier to restrict the release of flammable gases, inhibiting the contact between the combustible gases and the combustion zone, exhibiting a condensed phase flame-retardant mechanism. During the second burning section (above 450 °C), BP nanosheets begin to thermally decompose. Similar to red phosphorus, [7,35] BP exerts the double flame-retardant mechanism containing vapor phase and condensed phase in the combustion process. On the one hand, undecomposed BP may generate active radicals, such as PO•, PO_2•, and HPO•, which can scavenge H• and OH• radicals to decrease the production of inflammable products (Fig. 12) [59]. On the other hand, partial BP is primarily oxidized into P_xO_y and various phosphoric acid derivatives. These phosphoric acid derivatives will react with epoxy to form some new structures, such as O-P=O and P-O-P complexes (Fig. 14(e) and (f)), and accelerate the formation of char residues (Fig. 13(c) and (f)), which will suppress the release of flammable gases, heat transfer and smoke emissions (Fig. 11(b)-(f)), achieving a condense phase flame-retardant mechanism.

3.9. Thermal conductivity of EP composites

High-efficiency heat dissipation is critical for the use of polymer composites in electronic devices. Graphene, which is similar to BP, has a very high thermal conductivity and has been extensively studied in recent years. However, studies on the thermal conductivity of BP are very rare [60]. Therefore, studying the thermal conductivity of BP is conducive to open up a new application field of BP. In order to assess the thermal management of EP nanocomposites, the infrared thermal imager is employed to observe the temperature change. All the samples are placed on a LED light strip (24 W) at the same time, and then turn on the power, the changes of temperature are recorded during the heating and cooling process. As shown in Fig. 16(a), the temperature rises of EP/BP 3.0 and EP/RuL_3@BP 3.0 are significantly faster than that of pure EP during the heating process, owing to the enhancement of heat transfer by the ordered single crystal structure of BP. Especially, the heat transfer rate of EP/RuL_3@BP 3.0 is higher than that of EP/BP 3.0. After 30 s heating, the temperature of EP/RuL_3@BP 3.0 reaches 80.0 °C, while the temperature of EP/BP 3.0 and pure EP are only 73.7 °C and 51.9 °C, respectively. This result is completely consistent with the HRR curves (Fig. 11 (b)), after only 25 s burning, EP/RuL_3@BP 3.0 and EP/BP 3.0 show a high heat release rate, confirming that BP and RuL_3@BP have a very high heat transfer efficiency. The reason can be interpreted from two aspects. On the one hand, after the coordination of BP by RuL_3, the dispersibility of BP is enhanced, which is beneficial to the transfer of heat. On the other hand, the ruthenium has a thermal conductivity of 117 W m^{-1} k^{-1}, the thermal conductivity of the entire system can be improved by the coordination effect with BP. Fig. 16(b) shows the heating curves of EP nanocomposites. Obviously, the heating rate of EP/RuL_3@BP 3.0 is dramatically higher than that of pure EP, which indicates RuL_3@BP can effectively improve the heat transfer efficiency of composites. Meanwhile, the cooling process of the samples are also studied in Fig. 16(c) and (d). From Fig. 16 (c), the heat dissipation rate of EP/RuL_3@BP 3.0 is also highest than other samples, this result once again confirms that RuL_3@BP has a very high heat transfer rate. The cooling curves are exhibited in Fig. 16 (d). As we excepted, EP/RuL_3@BP 3.0 can cool down quickly from 80.0 °C to 39.0 °C in 60 s. However, the temperature of EP is still as high as

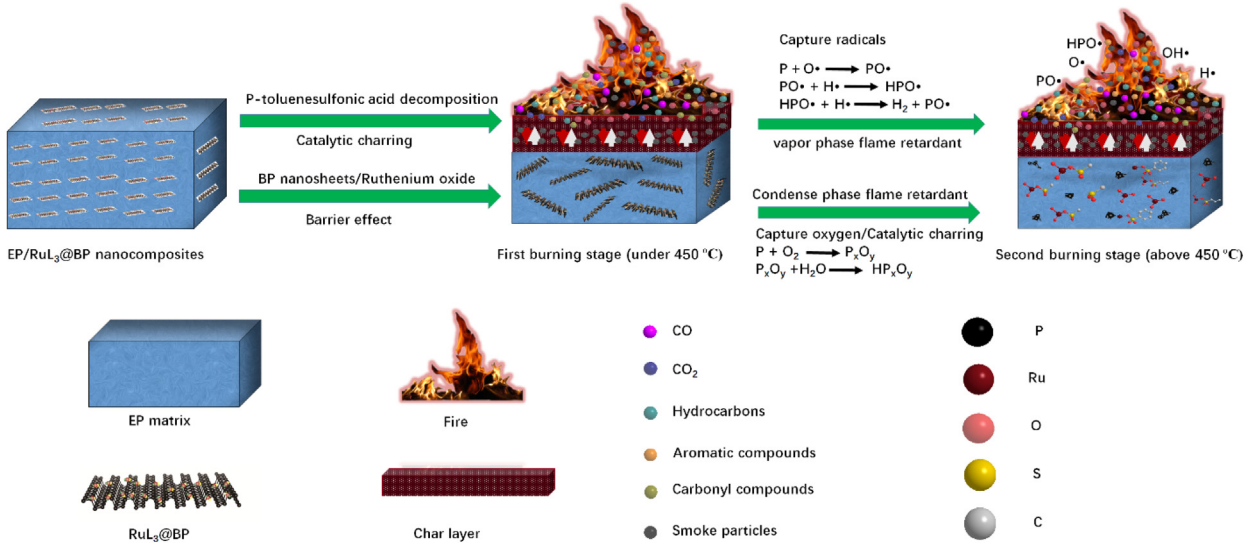

Fig. 15. Flame-retardant mechanism of RuL_3@ BP in epoxy.

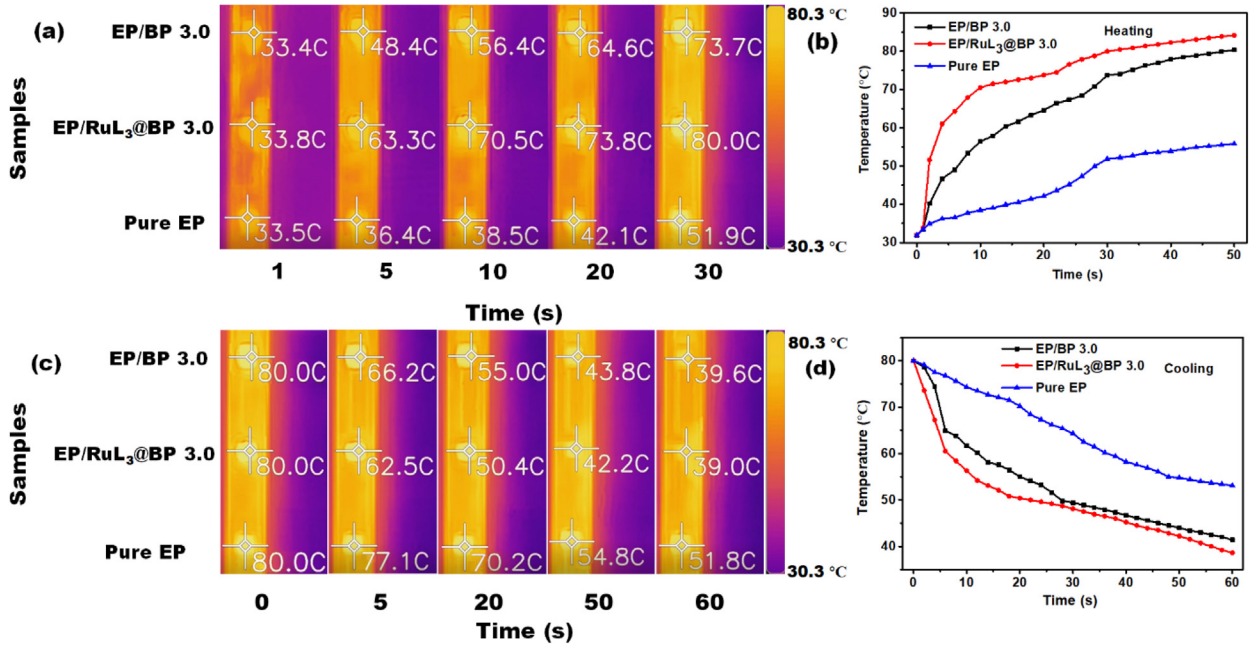

Fig. 16. Temperature changes of EP nanocomposites: (a) infrared thermal images of heating process; (b) temperature change curves of heating process; (c) infrared thermal images of cooling process; (d) temperature change curves of cooling process.

51.8 ˚C. All the results prove that the coordination of BP by RuL_3 is very advantageous to improve the heat transfer rate of epoxy resin.

An LFA 467 instrument is utilized to measure the thermal conductivity by the laser flash method, the specific data are exhibited in Table S5. Fig. 17(a) presents that RuL_3@BP can significantly enhance the thermal conductivity of EP. The thermal conductivity of pure EP is only 0.227 W m^{-1} K^{-1}, while that of EP/RuL_3@BP 1.0, EP/RuL_3@BP 2.0 and EP/RuL_3@BP 3.0 are as high as 0.257 W m^{-1} K^{-1}, 0.303 W m^{-1} K^{-1}, 0.376 W m^{-1} K^{-1}, respectively. With the loading of RuL_3@BP increasing from 1.0 to 3.0 wt%, the thermal conductivity is enhanced by 13.22–65.64%, which is higher than the same loading of graphene/mesogenic epoxy composites (about 35% enhancement) [61]. Nevertheless, the thermal conductivity of EP/BP 3.0 is only 0.247 W m^{-1} K^{-1} and its enhancement is just 8.81%, which is ascribed to the serious agglomeration of BP. Based on the above results, a possible thermal conductivity mechanism can be proposed in Fig. 17(b). Pure BP easily aggregates in epoxy (Fig. 8(a) and (c)), which is very unfavorable for heat transfer by phonon and cannot improve the interfacial interactions between BP and EP [41,62]. Compared with BP, after RuL_3 coordination, the dispersion of BP in the EP resin can be greatly improved (Fig. 8(b) and (d)), and the size of the filler will be smaller (Fig. 3(d)), which makes it possible to reduce the interfacial thermal resistance [63]. In addition, ruthenium itself has a high thermal conductivity, and its introduction naturally promotes the thermal conductivity of the composite.

4. Conclusion

In this work, a ruthenium sulfonate ligand (RuL_3) is fabricated to coordinate with few-layer BP to form RuL_3@BP via surface coordination strategy. The results of experiments confirm that RuL_3 is successful coordinated onto the BP surface. The P-Ru coordination improves the stability of BP in environment and different solvents by occupying the lone pair electrons of black phosphorus. The surface coordination effect can also significantly solve the aggregation phenomenon and enhance the dispersibility of BP nanosheets in epoxy. The resultant RuL_3@BP can effectively catalyze the curing of EP/RuL_3@BP nanocomposites. Incorporation of 3.0 wt% RuL_3@BP into EP exhibits high residual char rate and tensile strength. In addition, the LOI of EP/RuL_3@BP nanocomposites is obviously improved and its PHRR, THR, SPR, TSP and COP values are all significantly decreased, the nanocomposites can easily pass the UL-94 V-0 rating. TG-FTIR results indicate that all the

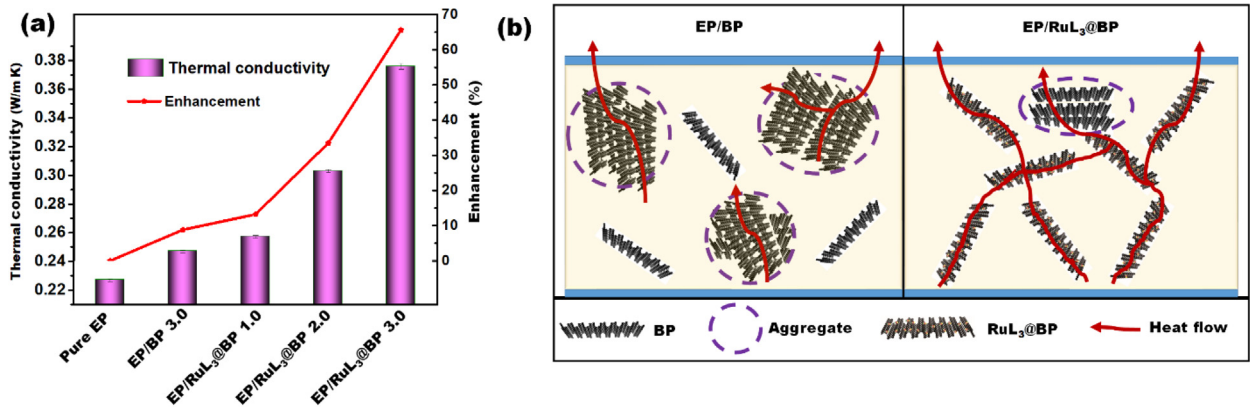

Fig. 17. (a) Thermal conductivity and the enhancement of thermal coefficient compared with pure EP; (b) thermal conductivity mechanism mold of EP/BP and EP/RuL_3@BP.

release of pyrolysis gases including CO are dramatically suppressed with the addition of RuL_3@BP. Characterization of residual char demonstrates that RuL_3@BP is favorable for the formation of a compact and dense char layer. A novel two-stage flame-retardant mechanism is proposed on the analysis of the vapor and condensed phase in combustion. Finally, the thermal conductivity and its mechanism of EP/RuL_3@BP nanocomposites are also studied, indicating RuL_3@BP has a high heat transfer efficiency. A simple, low addition and economical strategy for stability of BP, excellent flame-retardant efficiency and high thermal conductivity in epoxy is achieved in the study, and the surface coordination strategy will enhance the potential application of BP in many fields.

Declaration of Competing Interest

The authors declare that they have no known competing financial interests or personal relationships that could have appeared to influence the work reported in this paper.

Acknowledgements

This work was supported by National Key R&D Program of China (2017YFD0601003) and Science and Technology Planning Project of Guangzhou (201904010244).

Appendix A. Supplementary data

Supplementary data to this article can be found online at https://doi.org/10.1016/j.cej.2020.125416.

References

[1] H. Liu, Y. Du, Y. Deng, P.D. Ye, Semiconducting black phosphorus: synthesis, transport properties and electronic applications, Chem. Soc. Rev 44 (2015) 2732–2743.
[2] A. Favron, E. Gaufres, F. Fossard, A.L. Phaneuf-L'Heureux, N.Y. Tang, P.L. Levesque, A. Loiseau, R. Leonelli, S. Francoeur, R. Martel, Photooxidation and quantum confinement effects in exfoliated black phosphorus, Nat. Mater. 14 (2015) 826–832.
[3] J. Pang, A. Bachmatiuk, Y. Yin, B. Trzebicka, L. Zhao, L. Fu, R.G. Mendes, T. Gemming, Z. Liu, M.H. Rummeli, Applications of Phosphorene and Black Phosphorus in Energy Conversion and Storage Devices, Adv. Energy Mater. 8 (2018).
[4] Z. Luo, G. Qi, K. Chen, M. Zou, L. Yuwen, X. Zhang, W. Huang, L. Wang, Microwave-Assisted Preparation of White Fluorescent Graphene Quantum Dots as a Novel Phosphor for Enhanced White-Light-Emitting Diodes, Adv. Funct. Mater. 26 (2016) 2739–2744.
[5] X. Zhu, T. Zhang, Z. Sun, H. Chen, J. Guan, X. Chen, H. Ji, P. Du, S. Yang, Black Phosphorus Revisited: A Missing Metal-Free Elemental Photocatalyst for Visible Light Hydrogen Evolution, Adv. Mater. 29 (2017).
[6] Y. Mu, M.S. Si, The mechanical exfoliation mechanism of black phosphorus to phosphorene: A first-principles study, EPL (Europhys. Lett.) 112 (2015).
[7] S. Qiu, B. Zou, H. Sheng, W. Guo, J. Wang, Y. Zhao, W. Wang, R.K.K. Yuen, Y. Kan, Y. Hu, Electrochemically Exfoliated Functionalized Black Phosphorene and Its Polyurethane Acrylate Nanocomposites: Synthesis and Applications, ACS Appl. Mater. Interfaces 11 (2019) 13652–13664.
[8] J.R. Brent, N. Savjani, E.A. Lewis, S.J. Haigh, D.J. Lewis, P. O'Brien, Production of few-layer phosphorene by liquid exfoliation of black phosphorus, Chem. Commun. (Camb) 50 (2014) 13338–13341.
[9] Z. Shen, S. Sun, W. Wang, J. Liu, Z. Liu, J.C. Yu, A black–red phosphorus heterostructure for efficient visible-light-driven photocatalysis, J. Mater. Chem. A 3 (2015) 3285–3288.
[10] J. Sun, G. Zheng, H.W. Lee, N. Liu, H. Wang, H. Yao, W. Yang, Y. Cui, Formation of stable phosphorus-carbon bond for enhanced performance in black phosphorus nanoparticle-graphite composite battery anodes, Nano Lett. 14 (2014) 4573–4580.
[11] P. Yasaei, B. Kumar, T. Foroozan, C. Wang, M. Asadi, D. Tuschel, J.E. Indacochea, R.F. Klie, A. Salehi-Khojin, High-quality black phosphorus atomic layers by liquid-phase exfoliation, Adv. Mater. 27 (2015) 1887–1892.
[12] D. Hanlon, C. Backes, E. Doherty, C.S. Cucinotta, N.C. Berner, C. Boland, K. Lee, A. Harvey, P. Lynch, Z. Gholamvand, S. Zhang, K. Wang, G. Moynihan, A. Pokle, Q.M. Ramasse, N. McEvoy, W.J. Blau, J. Wang, G. Abellan, F. Hauke, A. Hirsch, S. Sanvito, D.D. O'Regan, G.S. Duesberg, V. Nicolosi, J.N. Coleman, Liquid exfoliation of solvent-stabilized few-layer black phosphorus for applications beyond electronics, Nat. Commun. 6 (2015) 8563.
[13] M. Lee, A.K. Roy, S. Jo, Y. Choi, A. Chae, B. Kim, S.Y. Park, I. In, Exfoliation of black phosphorus in ionic liquids, Nanotechnology 28 (2017) 125603.
[14] J.-H. Choi, P. Cui, W. Chen, J.-H. Cho, Z. Zhang, Atomistic mechanisms of van der Waals epitaxy and property optimization of layered materials, Wiley Interdisciplinary Rev. Comput. Mol. Sci. 7 (2017).
[15] X. Yu, H. Li, J. Zhou, Phonon thermal conductivity reduction in silicene nanotubes with isotope substitution, RSC Adv. 10 (2020) 10752–10757.
[16] X. Xin, Y. Song, S. Guo, Y. Zhang, B. Wang, Y. Wang, X. Li, One-step synthesis of P-doped MoS2 for efficient photocatalytic hydrogen production, J. Alloy. Compd. 829 (2020).
[17] H. Tian, Y. Yao, S. Ma, J. Wu, A. Xiang, Enhanced thermal stability and flame resistance of polyurethane-imide foams by adding silicon carbide, Adv. Polym. Tech. 37 (2018) 2470–2477.
[18] Y. Zhang, X. Rui, Y. Tang, Y. Liu, J. Wei, S. Chen, W.R. Leow, W. Li, Y. Liu, J. Deng, B. Ma, Q. Yan, X. Chen, Wet-Chemical Processing of Phosphorus Composite Nanosheets for High-Rate and High-Capacity Lithium-Ion Batteries, Adv. Energy Mater. 6 (2016).
[19] X. Ren, P. Lian, D. Xie, Y. Yang, Y. Mei, X. Huang, Z. Wang, X. Yin, Properties, preparation and application of black phosphorus/phosphorene for energy storage: a review, J. Mater. Sci. 52 (2017) 10364–10386.
[20] M.J. Nine, M.A. Cole, D.N.H. Tran, D. Losic, Graphene: a multipurpose material for protective coatings, J. Mater. Chem. A 3 (2015) 12580–12602.
[21] H. Guo, Y. Li, J. Zheng, J. Gan, L. Liang, K. Wu, M. Lu, Reinforcement in the mechanical properties of shape memory liquid crystalline epoxy composites, J. Appl. Polym. Sci. 132 (2015) n/a-n/a.
[22] J.D. Wood, S.A. Wells, D. Jariwala, K.S. Chen, E. Cho, V.K. Sangwan, X.L. Liu, L.J. Lauhon, T.J. Marks, M.C. Hersam, Effective Passivation of Exfoliated Black Phosphorus Transistors against Ambient Degradation, Nano Lett. 14 (2014) 6964–6970.
[23] J.S. Kim, Y.N. Liu, W.N. Zhu, S. Kim, D. Wu, L. Tao, A. Dodabalapur, K. Lai, D. Akinwande, Toward air-stable multilayer phosphorene thin-films and transistors, Sci Rep 5 (2015) 7.
[24] H.U. Lee, S.C. Lee, J.G. Won, B.C. Son, S.H. Choi, Y.S. Kim, S.Y. Park, H.S. Kim, Y.C. Lee, J. Lee, Stable semiconductor black phosphorus (BP)@titanium dioxide (TiO2) hybrid photocatalysts, Sci Rep 5 (2015) 6.
[25] H. Hu, H. Gao, L. Gao, F. Li, N. Xu, X. Long, Y. Hu, J. Jin, J. Ma, Covalent functionalization of black phosphorus nanoflakes by carbon free radicals for durable air and water stability, Nanoscale 10 (2018) 5834–5839.
[26] G. Abellan, V. Lloret, U. Mundloch, M. Marcia, C. Neiss, A. Gorling, M. Varela, F. Hauke, A. Hirsch, Noncovalent Functionalization of Black Phosphorus, Angew. Chem.-Int. Edit. 55 (2016) 14557–14562.
[27] Y. Zhao, H. Wang, H. Huang, Q. Xiao, Y. Xu, Z. Guo, H. Xie, J. Shao, Z. Sun, W. Han, X.F. Yu, P. Li, P.K. Chu, Surface Coordination of Black Phosphorus for Robust Air and Water Stability, Angew Chem Int Ed Engl 55 (2016) 5003–5007.
[28] J. Zhang, Q. Kong, D.-Y. Wang, Simultaneously improving the fire safety and mechanical properties of epoxy resin with Fe-CNTs via large-scale preparation, J. Mater. Chem. A 6 (2018) 6376–6386.
[29] J. Zhang, Q. Kong, L. Yang, D.-Y. Wang, Few layered Co(OH)2ultrathin nanosheet-based polyurethane nanocomposites with reduced fire hazard: from eco-friendly flame retardance to sustainable recycling, Green Chem. 18 (2016) 3066–3074.
[30] Q. Kong, Y. Sun, C. Zhang, H. Guan, J. Zhang, D.-Y. Wang, F. Zhang, Ultrathin iron phenyl phosphonate nanosheets with appropriate thermal stability for improving fire safety in epoxy, Compos. Sci. Technol. 182 (2019).
[31] Q. Kong, T. Wu, H. Zhang, Y. Zhang, M. Zhang, T. Si, L. Yang, J. Zhang, Improving flame retardancy of IFR/PP composites through the synergistic effect of organic montmorillonite intercalation cobalt hydroxides modified by acidified chitosan, Appl. Clay Sci. 146 (2017) 230–237.
[32] L. Liu, Y. Xu, M. Xu, Z. Li, Y. Hu, B. Li, Economical and facile synthesis of a highly efficient flame retardant for simultaneous improvement of fire retardancy, smoke suppression and moisture resistance of epoxy resins, Compos. B Eng. 167 (2019) 422–433.
[33] X. Ren, Y. Mei, P. Lian, D. Xie, Y. Yang, Y. Wang, Z. Wang, A Novel Application of Phosphorene as a Flame Retardant, Polymers (Basel) 10 (2018).
[34] X. Ren, Y. Mei, P. Lian, D. Xie, W. Deng, Y. Wen, Y. Luo, Fabrication and Application of Black Phosphorene/Graphene Composite Material as a Flame Retardant, Polymers (Basel) 11 (2019).
[35] S. Qiu, Y. Zhou, X. Zhou, T. Zhang, C. Wang, R.K.K. Yuen, W. Hu, Y. Hu, Air-Stable Polyphosphazene-Functionalized Few-Layer Black Phosphorene for Flame Retardancy of Epoxy Resins, Small 15 (2019) e1805175.
[36] L. Shao, H. Sun, L. Miao, X. Chen, M. Han, J. Sun, S. Liu, L. Li, F. Cheng, J. Chen, Facile preparation of NH2-functionalized black phosphorene for the electrocatalytic hydrogen evolution reaction, J. Mater. Chem. A 6 (2018) 2494–2499.
[37] J. Wang, D. Liu, H. Huang, N. Yang, B. Yu, M. Wen, X. Wang, P.K. Chu, X.F. Yu, In-Plane Black Phosphorus/Dicobalt Phosphide Heterostructure for Efficient Electrocatalysis, Angew Chem Int Ed Engl 57 (2018) 2600–2604.
[38] W. Lei, T. Zhang, P. Liu, J.A. Rodriguez, G. Liu, M. Liu, Bandgap- and Local Field-Dependent Photoactivity of Ag/Black Phosphorus Nanohybrids, ACS Catal. 6 (2016) 8009–8020.
[39] E.A. Lewis, J.R. Brent, B. Derby, S.J. Haigh, D.J. Lewis, Solution processing of two-dimensional black phosphorus, Chem. Commun. 53 (2017) 1445–1458.
[40] X. Wang, W. Xing, X. Feng, L. Song, Y. Hu, MoS2/Polymer Nanocomposites: Preparation, Properties, and Applications, Polym. Rev. 57 (2017) 440–466.
[41] C.-H. Chen, C.-M. Lin, T.-Y. Juang, M.M. Abu-Omar, C.-H. Lin, The reaction of activated esters with epoxides for self-curable, highly flexible, A2B2- and A3B3-type epoxy compounds, Polym. Chem. 10 (2019) 3983–3995.
[42] F. Xiao, K. Wu, F. Luo, Y. Guo, S. Zhang, X. Du, Q. Zhu, M. Lu, An efficient phosphonate-based ionic liquid on flame retardancy and mechanical property of epoxy resin, J. Mater. Sci. 52 (2017) 13992–14003.

[43] F. Luo, K. Wu, Y. Li, J. Zheng, H. Guo, M. Lu, Reactive flame retardant with core-shell structure and its flame retardancy in rigid polyurethane foam, J. Appl. Polym. Sci. 132 (2015) n/a-n/a.
[44] Y. Gao, J. Wu, Q. Wang, C.A. Wilkie, D. O'Hare, Flame retardant polymer/layered double hydroxide nanocomposites, J. Mater. Chem. A 2 (2014).
[45] B. Wicklein, A. Kocjan, G. Salazar-Alvarez, F. Carosio, G. Camino, M. Antonietti, L. Bergstrom, Thermally insulating and fire-retardant lightweight anisotropic foams based on nanocellulose and graphene oxide, Nat Nanotechnol 10 (2015) 277–283.
[46] X. Liu, S. Qin, H. Li, J. Sun, X. Gu, S. Zhang, J.C. Grunlan, Combination Intumescent and Kaolin-Filled Multilayer Nanocoatings that Reduce Polyurethane Flammability, Macromol. Mater. Eng. 304 (2018).
[47] Z. Qu, K. Wu, E. Jiao, W. Chen, Z. Hu, C. Xu, J. Shi, S. Wang, Z. Tan, Surface functionalization of few-layer black phosphorene and its flame retardancy in epoxy resin, Chem. Eng. J. (2019).
[48] F. Xiao, K. Wu, F. Luo, S. Yao, M. Lv, H. Zou, M. Lu, Influence of Ionic Liquid-Based Metal-Organic Hybrid on Thermal Degradation, Flame Retardancy, and Smoke Suppression Properties of Epoxy Resin Composites, J. Mater. Sci. 53 (2018) 10135–10146.
[49] S. Zhou, Z.Z. Wang, Z. Gui, Y. Hu, A Study of the Novel Intumescent Flame-Retarded PP/EPDM Copolymer Blends, J. Appl. Polym. Sci. 110 (2008) 3804–3811.
[50] K. Wu, Z. Wang, Y. Hu, Microencapsulated ammonium polyphosphate with urea-melamine-formaldehyde shell: preparation, characterization, and its flame retardance in polypropylene, Polym. Adv. Technol. 19 (2008) 1118–1125.
[51] J.-Z. Du, L. Jin, H.-Y. Zeng, B. Feng, S. Xu, E.-G. Zhou, X.-K. Shi, L. Liu, X. Hu, Facile preparation of an efficient flame retardant and its application in ethylene vinyl acetate, Appl. Clay Sci. 168 (2019) 96–105.
[52] N.N. Li, H.Q. Yan, L. Xia, L.B. Mao, Z.P. Fang, Y.H. Song, H. Wang, Flame retarding and reinforcing modification of ramie/polybenzoxazine composites by surface treatment of ramie fabric, Compos. Sci. Technol. 121 (2015) 82–88.
[53] X. Qian, L. Song, B. Yu, B. Wang, B. Yuan, Y. Shi, Y. Hu, R.K.K. Yuen, Novel organic–inorganic flame retardants containing exfoliated graphene: preparation and their performance on the flame retardancy of epoxy resins, J. Mater. Chem. A 1 (2013).
[54] Y. Shi, B. Yu, L. Duan, Z. Gui, B. Wang, Y. Hu, R.K.K. Yuen, Graphitic carbon nitride/phosphorus-rich aluminum phosphinates hybrids as smoke suppressants and flame retardants for polystyrene, J Hazard Mater 332 (2017) 87–96.
[55] S. Qiu, X. Wang, B. Yu, X. Feng, X. Mu, R.K.K. Yuen, Y. Hu, Flame-retardant-wrapped polyphosphazene nanotubes: A novel strategy for enhancing the flame retardancy and smoke toxicity suppression of epoxy resins, J Hazard Mater 325 (2017) 327–339.
[56] W.Z. Hu, B. Yu, S.D. Jiang, L. Song, Y. Hu, B.B. Wang, Hyper-branched polymer grafting graphene oxide as an effective flame retardant and smoke suppressant for polystyrene, J. Hazard. Mater. 300 (2015) 58–66.
[57] K.M. Shahil, A.A. Balandin, Graphene-multilayer graphene nanocomposites as highly efficient thermal interface materials, Nano Lett 12 (2012) 861–867.
[58] T. Zhang, Y. Wan, H. Xie, Y. Mu, P. Du, D. Wang, X. Wu, H. Ji, L. Wan, Degradation Chemistry and Stabilization of Exfoliated Few-Layer Black Phosphorus in Water, J Am Chem Soc 140 (2018) 7561–7567.
[59] L.L. Xu, L.H. Xiao, P. Jia, K. Goossens, P. Liu, H. Li, C.G. Cheng, Y. Huang, C.W. Bielawski, J.X. Geng, Lightweight and Ultrastrong Polymer Foams with Unusually Superior Flame Retardancy, ACS Appl. Mater. Interfaces 9 (2017) 26392–26399.
[60] S. Lee, F. Yang, J. Suh, S.J. Yang, Y. Lee, G. Li, H.S. Choe, A. Suslu, Y.B. Chen, C. Ko, J. Park, K. Liu, J.B. Li, K. Hippalgaonkar, J.J. Urban, S. Tongay, J.Q. Wu, Anisotropic in-plane thermal conductivity of black phosphorus nanoribbons at temperatures higher than 100 K, Nat. Commun. 6 (2015) 7.
[61] F. Luo, K. Wu, X. Huang, W. Hu, M. Lu, Encapsulation of Graphite Nanoflakes for Improving Thermal Conductivity of Mesogenic Epoxy Composites, Ind. Eng. Chem. Res. 56 (2017) 489–494.
[62] J. Zhu, H. Park, J.Y. Chen, X.K. Gu, H. Zhang, S. Karthikeyan, N. Wendel, S.A. Campbell, M. Dawber, X. Du, M. Li, J.P. Wang, R.G. Yang, X.J. Wang, Revealing the Origins of 3D Anisotropic Thermal Conductivities of Black Phosphorus, Adv. Electron. Mater. 2 (2016) 9.
[63] X.J. Liu, J.F. Gao, G. Zhang, Y.W. Zhang, Unusual Twisting Phonons and Breathing Modes in Tube-Terminated Phosphorene Nanoribbons and Their Effects on Thermal Conductivity, Adv. Funct. Mater. 27 (2017) 7.